Journal of Materials Research and Technology
Volume 18, 2022, Pages 2672-2698
https://doi.org/10.1016/j.jmrt.2022.03.170

Laser-powder bed fusion of silicon carbide reinforced 316L stainless steel using a sinusoidal laser scanning strategy

***Andre Mussatto**[1, 2, 3, a]**, Robert Groarke**[1, 2, 3]**, Rajani K. Vijayaraghavan**[2, 3, 4]**, Muhannad Ahmed Obeidi**[1, 2, 3]**, Patrick J. McNally**[2, 3, 4]**, Valeria Nicolosi**[5, 6, 7]**, Yan Delaure**[1, 2, 3]**, Dermot Brabazon**[1, 2, 3]*

[1] School of Mechanical and Manufacturing Engineering, Dublin City University, Glasnevin, Ireland

[2] I-Form Advanced Manufacturing Research Centre, Dublin City University, Glasnevin, Ireland

[3] Advanced Processing Technology Research Centre, Dublin City University, Glasnevin, Ireland

[4] School of Electronic Engineering, Dublin City University, Glasnevin, Ireland

[5] I-Form Advanced Manufacturing Research Centre, Trinity College Dublin, Dublin, Ireland

[6] Centre for Research on Adaptive Nanostructures and Nanodevices (CRANN) and Advanced Materials and Bioengineering Research (AMBER), Trinity College Dublin, Dublin, Ireland

[7] School of Chemistry, Trinity College Dublin, Dublin, Ireland

[a] Corresponding author: andre.mussatto2@mail.dcu.ie

Highlights

- A novel hatching pattern for laser-powder bed fusion of metal matrix composites is introduced.
- A method for improving mechanical properties and achieving texture control is investigated
- The tribological and mechanical properties of naturally formed oxide films are studied.
- A method for reducing process lead time and energy consumption is presented.

Abstract

Laser-powder bed fusion was identified as a promising technique for manufacturing metal matrix composites. However, over a decade later, little progress has been made in addressing the persisting issues hindering the wider exploitation and industrial usage of metal matrix composites. Therefore, the present study proposes the implementation of a feasible solution to accomplish research advancements in metal matrix composites. Where, the issues concerning their performance and cost have driven this study towards the development of a novel scanning strategy. A hatching system based on a sine wave was successfully developed and employed in the printing of metal matrix composites. Composites printed using the sinusoidal hatching exhibited an enhanced yield strength and ductility owing to the resultant grain refinement and texture. The dabber mode formation of material tracks promoted the growth of highly oriented intragranular cellular structures. Apart for playing an important role at the obtained hardness, this control over the cellular growth could also be used towards improving composite toughness. Additionally, besides improving composite performance, the sinusoidal hatching was also effective in reducing manufacturing lead time and process energy consumption.

Journal of Materials Research and Technology
Volume 18, 2022, Pages 2672-2698
https://doi.org/10.1016/j.jmrt.2022.03.170

Graphical Abstract

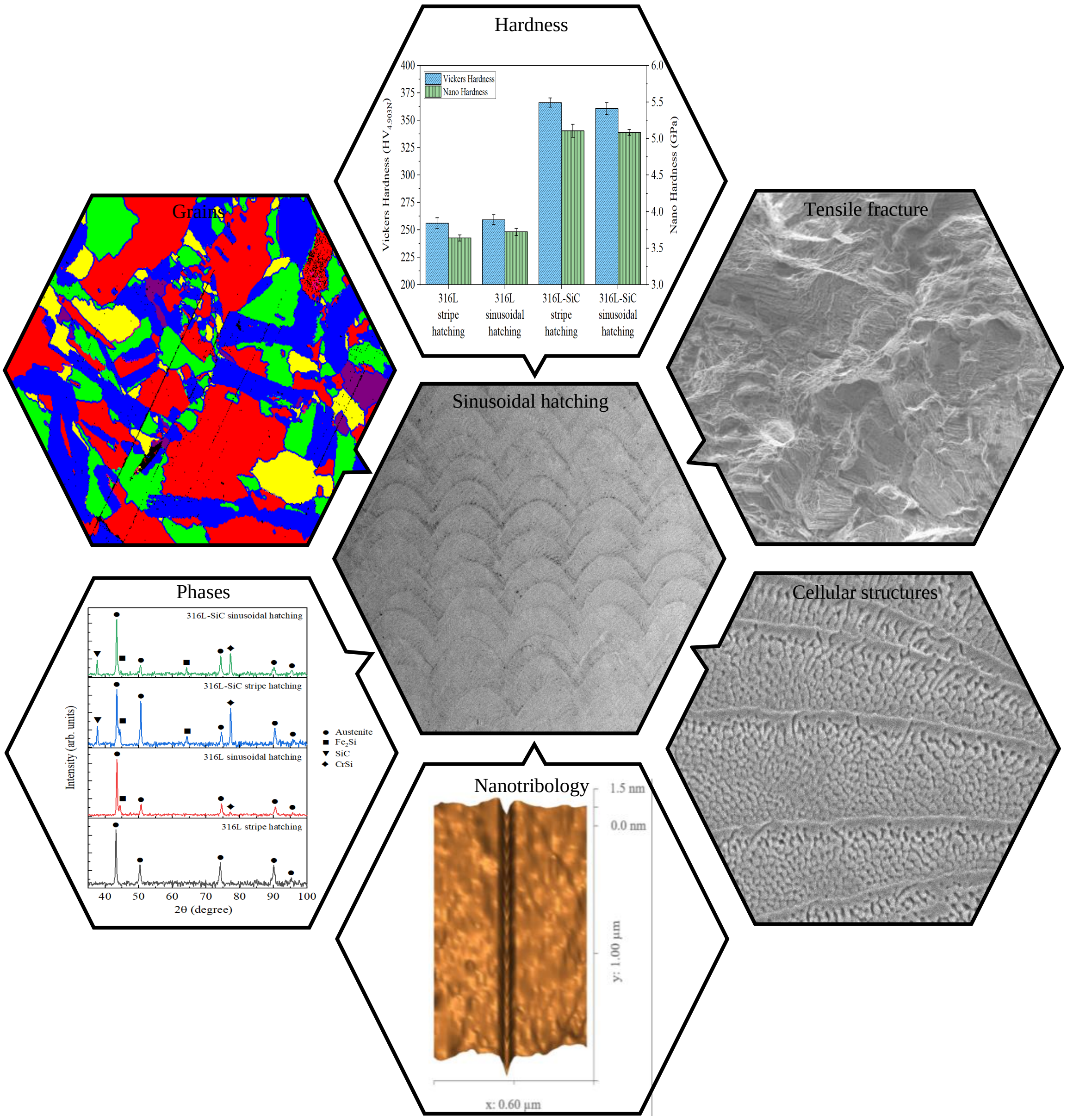

Keywords: powder bed fusion; sinusoidal scanning strategy; metal matrix composite; microstructure; nanotribology

1. Introduction

In many modern technological applications, components are very often required to have properties which are only possible by combining different materials, as against monolithic options individually [1]. Metal matrix composites (MMCs) are considered advanced materials due to the growing interest on them in the past decades in various high-performance applications such as those in the automotive and aerospace sectors [2,3]. Although MMCs have been used and are excellent candidate materials for advanced engineering systems, several aspects are hindering their further applications [3]. To which two of the possible reasons are their ductility and toughness achievements to date, and these properties' behavior in the presence of and with the increasing amount of reinforcement [4]. Technical challenges including inhomogeneous reinforcement dispersion, low wettability, deleterious interfacial reaction, weak interfacial bonding, porosity and micro defects are well known to have a major impact on the properties of MMCs [5–11]. Another challenge of MMCs is the availability of a suitable processing technique to extract the maximum reinforcement benefits [12]. Ease of processing, adequate economic efficiency, low energy consumption and complex net-shape ability are also process related aspects to consider [3,13–15]. Even though substantial research is still needed, in specific applications, the MMCs property-profiles are distinguished from metals and alloys by offering a gain in performance. Yet, as far as industries are concerned, the viability of MMCs depends on the balance between their performance and cost [16].

As aforementioned, the production of MMCs via conventional manufacturing techniques face several challenges and limitations. Rapidly becoming more and more popular, laser-powder bed fusion (L-PBF), which is suitable for obtaining ultrafine, gradient and pointwise-controlled microstructure, has been used for the production of both in-situ and ex-situ MMCs [13,3,17]. L-PBF offers an exceptional flexibility for producing functional geometrically complex dense composites, besides allowing unprecedented freedom of design and customisation [18]. It provides also an opportunity for producing MMCs with a homogeneous dispersion of reinforcement and material pairings free from limitations which is extremely important when developing new materials [19,20]. Recently, L-PBF was identified as the most promising technique to process MMCs as it has been showing the potential of addressing several of the current issues concerning MMC production, including manufacturing costs, waste and lead time [21,22]. However, while there is promises, and the fact that L-PBF is still in its infancy, its true and full potential for MMCs are yet to be discovered.

To date, little research into L-PBF of silicon carbide (SiC) reinforced 316L composites exists. From these, it was reported that SiC additions affect microstructural morphology and texture, and improve the composite strength due to the grain boundary, Orowan, dislocation and load transfer strengthening mechanisms [23]. However, densification was reported to be affected by the SiC addition because of porosity. High residual stresses due to coefficient of thermal expansion mismatch between phases caused micro cracks, hence reduced the ductility in composites [23]. The decomposition of SiC encouraged the formation of iron and chromium silicide phases, and these were found to help to decrease the mechanical strength of MMCs [24]. The decomposition of dispersed SiC particles is a common phenomenon in L-PBF synthetised iron-based composites [25–27]. Although the decomposition of SiC is generally seen as deleterious for the strength properties, modification of the matrix with Si and C atoms can activate processes like solid solution strengthening [28]. On the other hand, the incorporation of high amounts of SiC can reduce its decomposition as the 316L matrix saturates with Si and C atoms [29]. However, in this case the ductility of the matrix is compromised and the microstructure is more prone to cracks and porosities [23,30].

In L-PBF, the spatial moving pattern of the energy beam is regarded as scanning strategy. This parameter is known to have an influence on the building time and properties of printed components [31–33]. The most common, not necessarily commercially available, filling patterns are stripes, islands (i.e. based on stripes, hexagons and chessboard), grid zigzag, square spiral and contour offset [34–37]. Additionally, despite their limitations, fractal patterns such as the Hilbert and Peano-Gosper have been used as a method of reducing thermal gradients and residual stresses [38,39]. Unfortunately, all of these aforementioned infill patterns have one thing in common and this is the fact that their resulting scanning paths are linear. Hence, the generation of the nature inspired and custom scanning strategies, which are very often more suitable for components with complex geometries/features or is required to avoid printing defects and or to achieve a desirable component property value, is limited by this factor. Unfortunately, current commercial slicer softwares do not implicitly enable generation of such laser paths. Bo et al. [40] developed a helix scanning strategy based on the Voronoi diagram of the model slice and the recursive generation of toolpath algorithm for an engine impeller aiming to reduce the shape deformation magnitude and residual stress profiles. Similarly, the equidistant scanning algorithm was claimed to improve processing efficiency and component quality [41]. In fact, several other path generation algorithms that might be suitable for developing new scanning strategies can be found in the literature [37,42–46].

In this work, a specially developed powder mixture having a high flowability and spreadability performance was used for L-PBF of MMCs. A novel scanning strategy, here named sinusoidal hatching, was developed and used during the printing process in an attempt to improve the composites tensile properties and control crystallographic texture. Additionally, this scanning strategy was also explored as a feasible solution to some of the aforementioned issues faced by MMCs.

2. Experimental

2.1 Material and Sample Preparation

The characteristics and performance of the powder mixture developed for this work is presented in our previous studies [47,48]. The powder mixture is composed of a free-flowing gas atomised (35-50 µm) stainless steel 316L powder and a high purity (45-65 nm) SiC powder, obtained from Mimete S.r.l and US Research Nanomaterials Inc. Figure 1 shows the prepared powder mixture (316L + 1 wt.% of SiC) which is characterised by the cohesive SiC nanoparticles adhering and evenly decorating the surface of 316L particles.

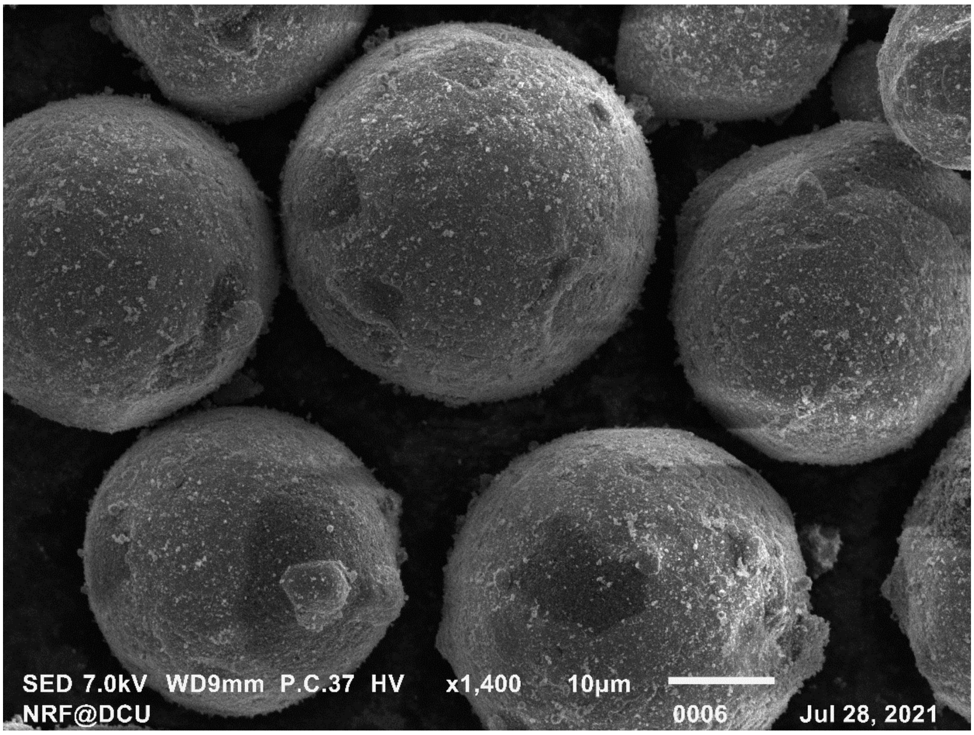

Figure 1 Micrograph of the prepared Nano-SiC satellited 316L feedstock powder.

The scanning strategies used in this work are illustrated in Figure 2. For generating the stripe hatching, models of the specimens were designed using SolidWorks and then the hatching was generated using a commercially available slicing tool, Netfabb Autodesk. While for the sinusoidal hatching, the three-dimensional design of the specimens and slicing were generated using a sine function, Excel Macro and JavaScript, then converted into Common Layer Interface. The inert gas (argon) flow was set perpendicular to hatching. Additionally, in order to reduce heat concentration zones, unidirectional scanning of the laser paths was considered.

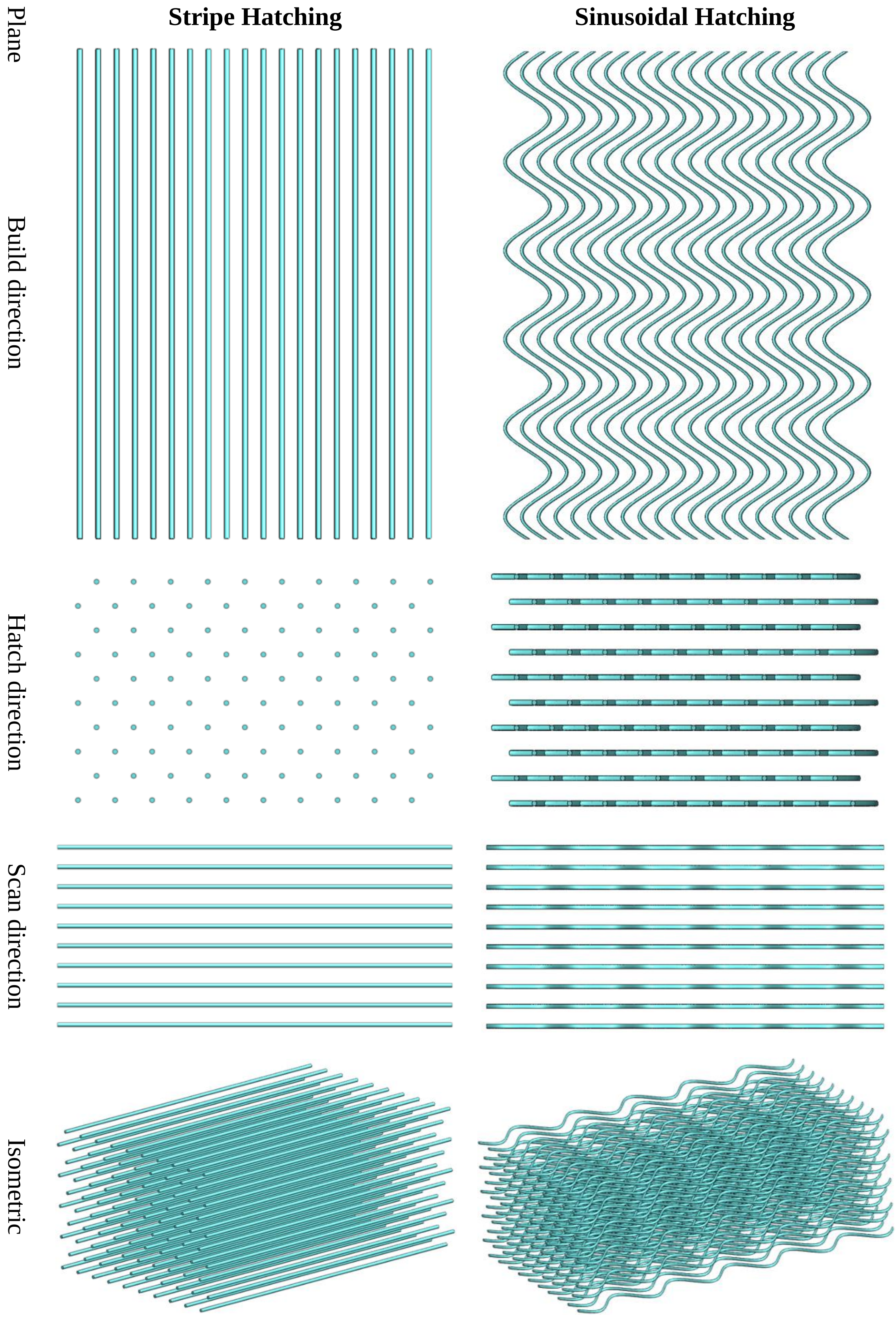

Figure 2 Illustration of the hatching systems used in this work.

Using an Aconity Mini (Aconity GmbH, Germany), cuboids and pins were printed based on the following design: 316L stripe hatching, 316L sinusoidal hatching, 316L-SiC stripe hatching and 316L-SiC sinusoidal hatching. The prints were repeated three times to enable verifying the results and to estimate the experimental variability. To avoid property variability, caused by the location parameter, specimens were only printed in the centre of the build platform [49]. The laser power and scanning speed for each individual hatching were established from a processing window obtained prior printing the specimens through single track experiments. Categorised by the hatching system, the processing parameters used during the printing of the specimens are listed in Table 1. As the printed specimens were to be either machined or ground (and polished) for characterisation, the contour laser scanning was not employed in this study.

Table 1 Processing parameters.

Parameter	Stripe Hatching	Sinusoidal Hatching
Laser power (W)	180	50
Scanning speed (mm/s)	600	10000
Laser beam diameter (µm)	50	50
Layer thickness (µm)	50	50
Hatch spacing (µm)	75	75
Hatch translation per layer (µm)	37.5	37.5
Amplitude (µm)	-	50
Period (µm)	-	200

2.2 Sample Characterisation

The density of the specimens was determined by means of densimetry based on Archimedes' principle (density scale Avery Berkel FA215DT and Sartorius YDK01 Density Determination Kit). Deionised water (at room temperature) was used as the immersion liquid while determining the density. The Vickers hardness was measured using a Leitz microhardness tester and the measurements were performed according to ASTM E92 standard [50]. A nanoindenter (Bruker Hysitron TI Premier, USA) equipped with a standard Berkovich diamond indenter was used for nanohardness measurement of the specimens. An array of 6x14 nanoindentations was performed with 10 mN load and intervals of 30 µm between indentations. The horizontally printed pins were machined to dimensions according to the ASTM E8 standard round Specimen 4 [51]. The tensile test was performed using a Zwick Z050 (Zwick/Roell GmbH, Germany) fitted with Zwick TestXpert software and equipped with an Epsilon clip-on extensometer model 3542 of a 10 mm gauge length. The used tensile testing speed was 3 mm/min. Nanoscratch tests were performed in a Bruker Dimension Icon atomic force microscope equipped with a NanoScope V controller and using a single crystal diamond tip (AD-40-SS) from Adama Innovations. A micrograph of the tip is available in Figure 3. First, the probe's deflection sensitivity of 60.47 nm/V and its cantilever spring constant of 54.13 N/m were determined by the thermal tune method. Then, single pass scratches were performed in contact mode with an applied normal force of 1 µN and tip lateral velocity of 1 µm/s. A Zeiss Evo LS15 and a JEOL JSM-IT100 scanning electron microscope (SEM) were used to obtain microstructural data. The microstructure was also investigated using a tripleaxis Jordan Valley Bede D1 high resolution X-ray diffraction (HR-XRD) system with a copper ($\lambda = 1.5405$ Å) radiation source operated at 45 kV and 40 mA, and a Zeiss Supra 40 field emission scanning electron microscope equipped with a Bruker e-FlashHR electron backscatter diffraction detector. Lastly, a Zeiss EVO LS-15 SEM equipped with a Xplore 15 detector from Oxford Instruments was utilised for elemental analysis.

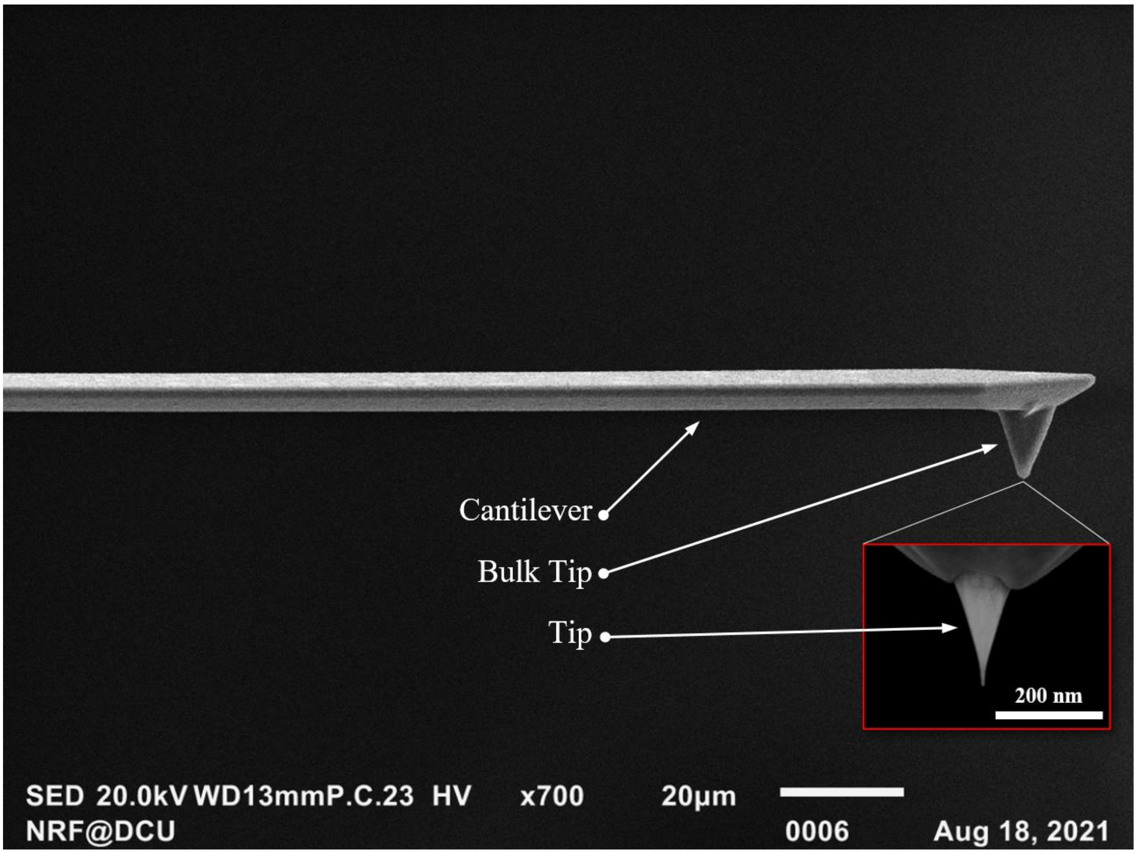

Figure 3 Single crystal diamond atomic force microscopy probe used in the nanoscratch testing.

3. Results

3.1 Density

The density of the printed specimens is presented in Figure 4. In order to properly assess the specimen's densities, the density of the virgin powders was also measured. Using a Micromeritics AccuPyc 1330 Helium pycnometer, densities of 7.75 and 3.16 g/cm^3 were confirmed for the 316L and SiC powder. Based on this it would be expected a 100 % dense unreinforced and reinforced specimen to have 7.75 and7.70 g/cm^3. However, the densities reported in Figure 4 suggest the presence of internal defect in the specimens. It is clear that, independently of the hatching system, the presence of nano SiC particles have promoted specimen densification. It is also seen that in comparison with the stripe hatching, those specimens printed using sinusoidal hatching showed a drop in density.

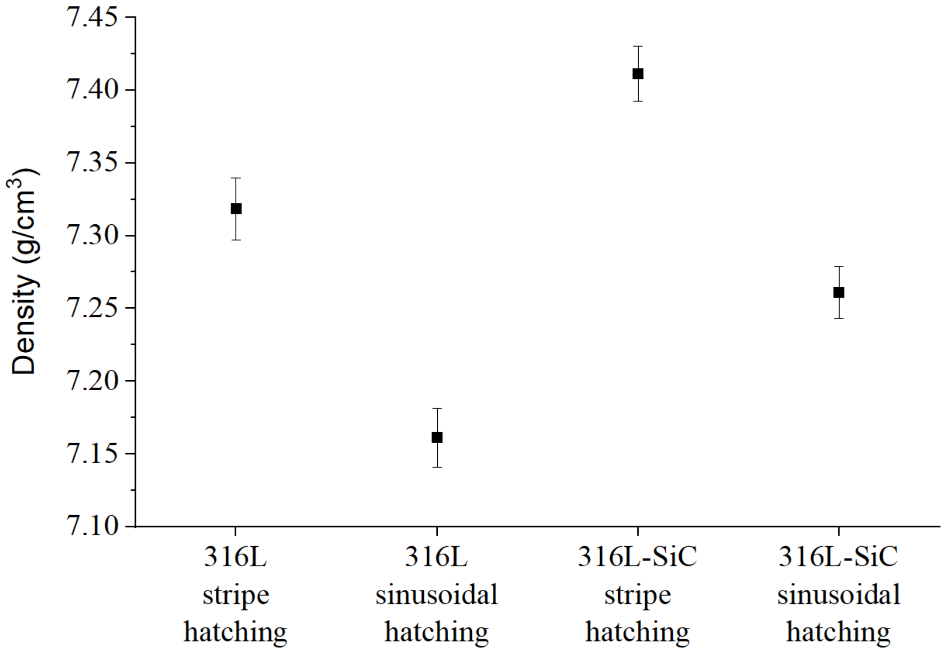

Figure 4 Compares the densities measured from the printed specimens. The data whiskers represent the 95% confidence interval.

3.2 Hardness

The hardness of the specimens measured from the plane perpendicular to the build direction is presented in Figure 5. The lower penetration depth, in the load-depth plot, corresponds to higher hardness, Figure 5a. It is worth noting that the micro and nanohardness have shown similar trend. The hardness of the 316L sinusoidal hatched specimen is slightly higher than that of the stripe hatched specimen. Regardless of this, based on previous studies, here both the micro [52,53] and nanohardness [54,55] holds a degree of improvement. The addition of 1 wt. % SiC has improve the hardness of the base material by approximately 30 %. A similar study also reporting the L-PBF of 316L-SiC claimed 347 HV for their 1.278 wt. % reinforced composite [23]. Therefore, despite using less reinforcement, the composites here printed presented higher hardness. Clearly, the hardness of the specimens can be related to their yield strength and elastic modulus, as well as their reduced modulus, Figure 5c. Factors such as grain size and the presence of residual stresses associated to the L-PBF process could be contributing to the seen hardness improvements.

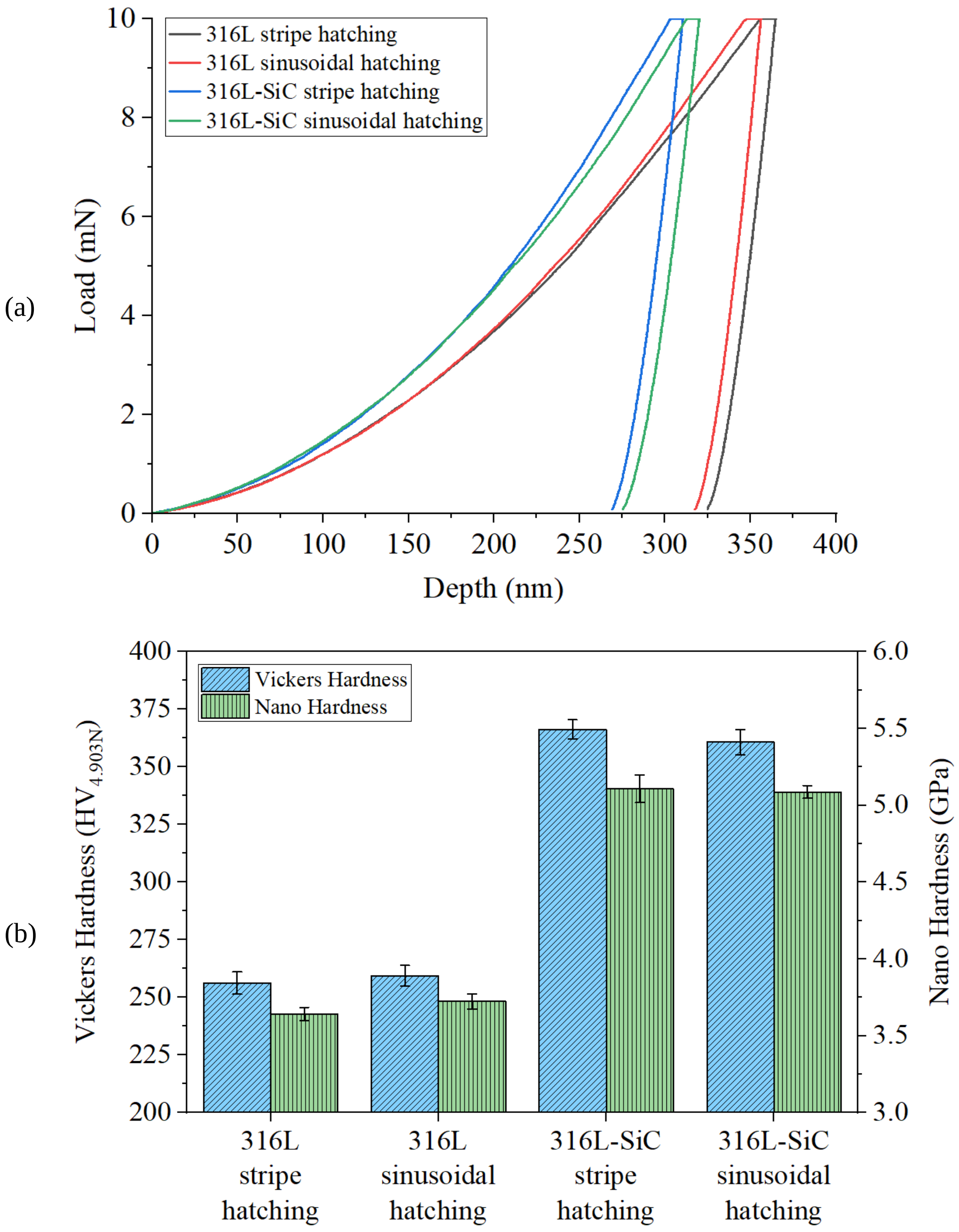

(c)

Specimen	**Reduced Modulus (GPa)**
316L stripe hatching	$194.05_{\pm 1.81}$
316L sinusoidal hatching	$195.07_{\pm 2.45}$
316L-SiC stripe hatching	$206.91_{\pm 1.44}$
316L-SiC sinusoidal hatching	$204.81_{\pm 2.03}$

Figure 5 Measured Vickers and nanoindentation data: (a) nanoindentation load-displacement curves, (b) micro and nanohardness and (c) reduced modulus. The data bounds noted are 95% confidence intervals.

3.3 Tensile Properties

The tensile properties extracted from the specimens while applying tension along the scanning direction are shown in Figure 6. Figure 6a shows that the 316L specimen printed using the stripe hatching exhibited the highest elongation at fracture. In comparison to the 316L sinusoidal hatching, this specimen also holds superior tensile properties, Figure 6b. The addition of SiC led to an increase in yield strength, ultimate tensile strength and elastic modulus of the base material. However, the enhancement of these properties was accompanied by a loss of ductility. Notably, the sinusoidal hatching system provided a positive effect on the tensile properties of the composite. Where in contrast with the composite printed using the stripe hatching, this composite presented superior tensile strength and ductility. Despite the used input process parameters had been established through single track screening, one should note that the tensile properties of the specimens were influenced by their low density, which is related to the presence of porosities and lack of fusion defects. Future research should therefore adopt a statistical approach for further optimisation of the input process parameters. A recent study reported that tighter overlap of melt pools (hatch spacing) is required to ensure enough heat accumulation for bonding between tracks, and so to increase specimen densification [56]. Also, the preheating of the powder bed to a temperature of 200 °C can be used to improve the heat absorptivity of the powder, aiding to the complete melting of powder. Additionally, laser rescanning (remelting) was reported to improve specimen densification [57]. Therefore, for specimens in which density may be critical for crack formation and propagation, an increased melt pool overlap, the incorporation of powder bed preheating and layer remelting may be employed.

(a)

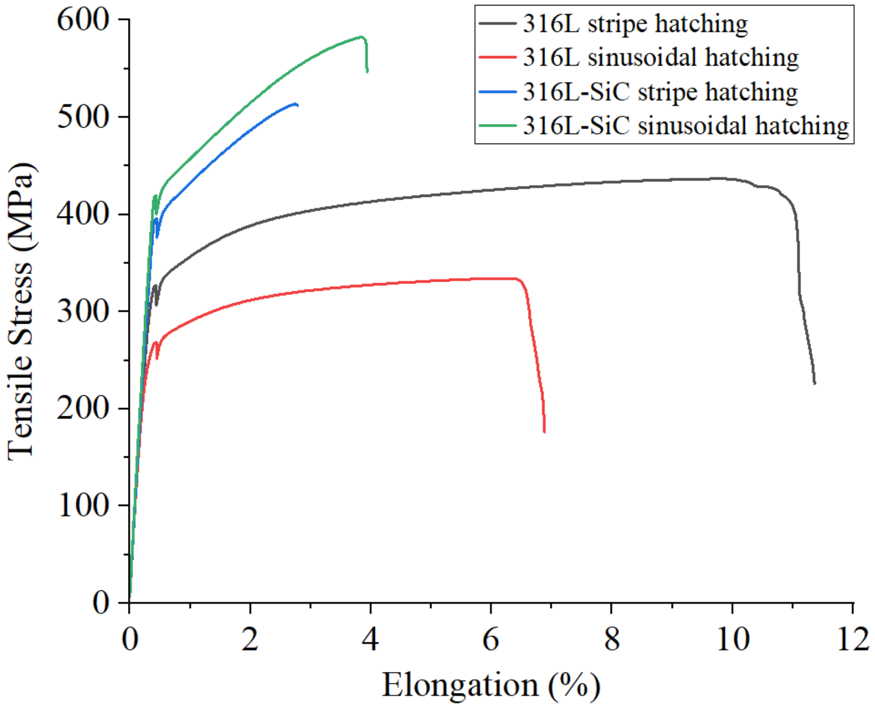

(b)

Specimen	**UTS (MPa)**	**YS (MPa)**	**E (GPa)**
316L stripe hatching	$431.82_{\pm 3.68}$	$343.37_{\pm 4.80}$	$131.93_{\pm 2.36}$
316L sinusoidal hatching	$330.17_{\pm 7.87}$	$278.78_{\pm 2.67}$	$126.86_{\pm 2.04}$
316L-SiC stripe hatching	$514.48_{\pm 3.26}$	$414.25_{\pm 2.73}$	$137.08_{\pm 2.51}$
316L-SiC sinusoidal hatching	$561.01_{\pm 15.86}$	$445.79_{\pm 4.05}$	$147.67_{\pm 2.79}$

Figure 6 Tensile performance of the specimens: (a) tensile stress versus percent elongation curves and (b) ultimate tensile strength, yield strength and elastic modulus. The data bounds noted are 95% confidence intervals.

Fractural analysis on the specimens was conducted using SEM observation, as shown in Figure 7. The existing porosities was considered as a particularly adverse factor for the tensile performance of the specimens as they contributed to and accelerated void growth and crack propagation causing premature fractures and failure under the tensile loads. The specimen of Figure 7a shows a ductile fracture in the presence of shear lips, whereas the specimen of Figure 7b shows almost no necking and a slanted fracture path indicating failure by ductility tearing from void coalescence induced microcracks [58]. Both of these specimens exhibited relative uniform dimpled fracture surfaces, with small dimples (around 1 µm in diameter) visible throughout the surfaces. Therefore, this suggests the existence of a subgrain structure, which affected the nucleation and growth of microvoids. The fracture morphologies of the composite specimens are shown in Figure 7c and 7d. The seen cleavage facets indicate that a brittle fracture process was developed during the failure due to the presence of the reinforcing brittle second phases. Despite the presence of brittle second phases, the composite of Figure 7d printed using the sinusoidal hatching also shows the presence of dimple patches, hence both brittle and ductile fracture characteristics were observed in this composite. Therefore, this resulted in the consumption of more plastic deformation, which is also reflected on the maximum elongation before failure between the two hatching systems seen in Figure 6 for the composite specimens.

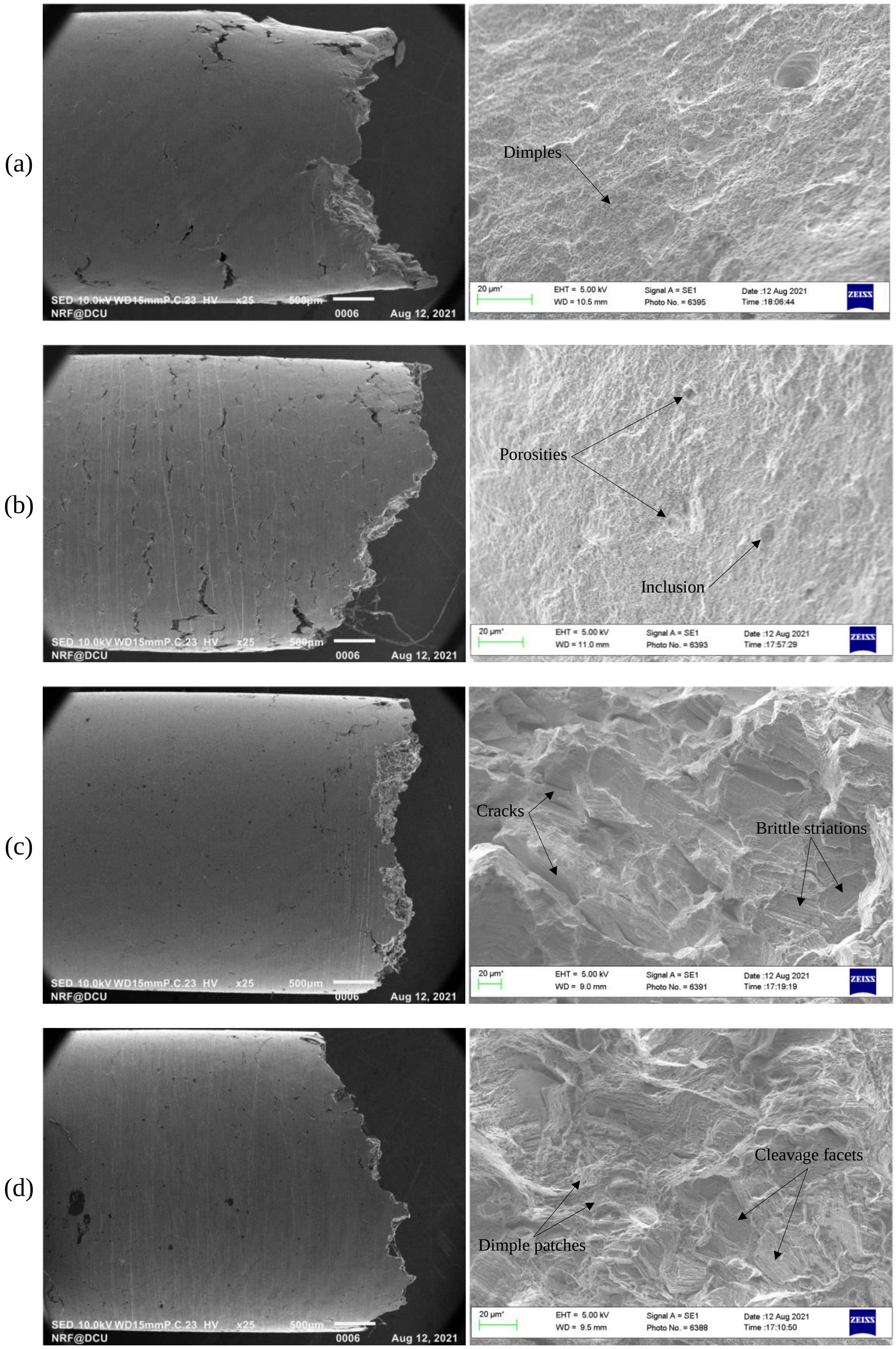

Figure 7 Tensile fracture characteristics of the specimen (a) 316L stripe hatching, (b) 316L sinusoidal hatching, (c) 316L-SiC stripe hatching and (d) 316L-SiC sinusoidal hatching.

3.4 Microstructure

Figure 8 shows the microstructure of the specimens with reference to the build plane, which was revealed after electrolytic etching for 30 s at 0.3 A/cm^2 with a 50 % HNO_3 solution. The etching also revealed the meltpools and their behaviour, but only in the unreinforced 316L specimens. Fine columnar grain bands observed from the specimen of Figure 8a were abruptly terminated at meltpool boundaries. Hence, it is possible that they have grown oriented towards the build direction. On the other hand, specimens of Figure 8a-c contained more complex columnar structures. Internal structure of columnar grains consists of colonies of cells [59]. In which, depending on growth direction, cells were either equiaxed or elongated [60]. This cellular structure is better observed in the high magnification micrographs of Figure 8, and they were formed because of complex heat transfer and large temperature gradients in the meltpool inherited from the ultrafast melting and solidification rates during laser processing. The highest temperature gradient is located on the bottom surface of concave shaped meltpools. Where, solidification of cellular structures starts perpendicular from the boundaries towards the centre of meltpools. Hence, cells are most likely to be oriented with its longitudinal direction parallel to the build direction. Whereas cells formed near the top of the meltpool boundaries can grow horizontally in response to the maximum heat flux direction. However, typically the structures formed on the top of meltpools are remelted during the fusion of the consecutive layer. Fluid dynamics of the meltpool driven by gas expansion and material evaporation, resulting from the recoil pressure [61] and the Marangoni flow effect on heat and mass transfer [62], can alter the heat flux direction. This is one of the reasons for the seen horizontal and arbitrary oriented colonies of cells. An example of a such complex growth behaviour was also observed on discontinuous meltpools, Figure 8a. Interestingly, colonies near the meltpool tip are oriented radially perpendicular to the tip planar boundary. A similar growth behaviour was also observed in Pham et al. single track study [63]. Therefore, it can be confirmed that the cells growth axis is closely perpendicular to the solid-liquid interface due to higher local thermal gradients and the maximum heat flux [64,65].

As illustrated in Figure 8b, the rapid rastering of the laser beam trough the sinusoidal path led to the formation of meltpools which have a “stack of dimes” type of look resembling weave bead patterns sometimes seen in metal welding [66–68], where each semicircle corresponds to a dab of filler formed during the welding [69]. The seen overlapping dabs resulted, therefore, from a dabber mode formation of material tracks. Factors such as laser, scanning and layer parameters and physical properties of the molten material such as surface tension and viscosity contribute to the spacing of the dabs. In contrast with the continuous mode, this interrupted action allowed for a faster cooling causing grain refinement and strong vertical texture. However, some grains persisted to go through multiple dabs, implying that the dabber mode does not completely prevent grains from elongating. Nevertheless, the colonies seen in this specimen are several orders of magnitude smaller than those of Figure 8a. The nonhomogeneous size of the refined structures seen in Figure 8c and 8**Figure 8**d resulted from the addition of SiC to 316L. Where, the degree of constitutional undercooling set by the composite composition, the distribution of SiC and thermal profiles in the liquid were associated with this phenomenon [70–72]. Therefore, based on the unreinforced specimens, here, those colonies decorated with slightly large structures correspond to a reinforcing phase. The observed porosity is probably associated with typical L-PBF defects, 316L, SiC and contaminants [73,74]. Therefore, the causes of porosity formation were either from entrapped gases (or absorption of surrounding gases), evaporation of certain elements, meltpool instabilities, shrinkage during solidification or other influencing factors such as powder humidity and oxygen content in the processing chamber. It is worth noting that pores were only found between grains, and where they resided there was a lack of grain boundary. Generally, solidification crack occurs along the grain boundaries and precipitated phases, aided by existing internal defects. Here, the presence of porosities made the specimens less ductile and offered an alternative pathway for crack to propagate. Cracking along cellular boundary is convoluted and often consumes more energy. In accordance with a previous study [75], fewer cracks were observed when using a relative high scanning speed. The 10000 mm/s scanning speed reduced the solidification time, which constrained aggregation of nano SiC particles and consequently reduced the degree of cracks. However, based on the density results of Figure 4, the increase in scanning speed correlated with an increase in porosity. Nevertheless, the tensile results of Figure 6 confirmed that higher scanning speed reflects on improvements in composite tensile strength and ductility.

Journal of Materials Research and Technology
Volume 18, 2022, Pages 2672-2698
https://doi.org/10.1016/j.jmrt.2022.03.170

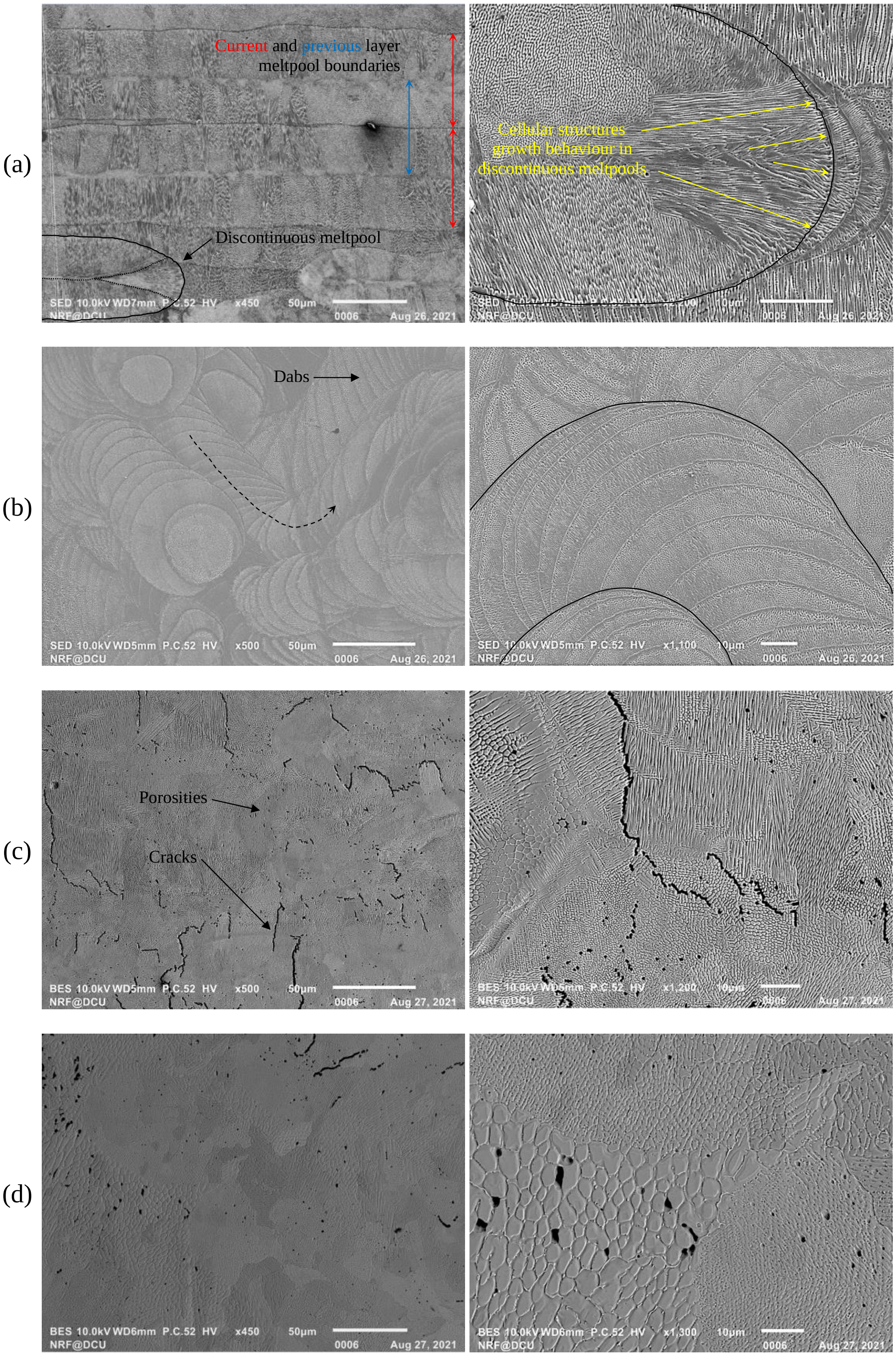

Figure 8 Microstructure of the specimen (a) 316L stripe hatching, (b) 316L sinusoidal hatching, (c) 316L-SiC stripe hatching and (d) 316L-SiC sinusoidal hatching.

3.5 Nanotribological Properties

The performance of metal matrix composite components such as engine pistons, valves and gas turbine blades also depends on the asperities, friction, wear, corrosion and lubricant properties of theirs exposed or contact surfaces with other metals, fluids and gases [76,77]. The surface of stainless steel is chemically reactive forming oxide layers in air and in other environments (i.e. chlorides, sulphides and nitrides). Some oxides are very tenacious, and the surface become passivated with no further oxidation. However, others like Fe_2O_3 can continue to grow in a humid air environment. Typically, the oxide layer ranges from 1 to 10 nm, which is established within a few minutes of exposure of atomic clean surface. Tribological oxidation is said to reduce the shear strength of the interface, which reduces wear and lower friction, and may effectively separate two contact surfaces [78]. However, at a high load and temperature, the oxide film may be penetrated. Then, transition to a high friction and wear occurs. Therefore, to develop fundamental understanding of the friction and wear properties of the naturally formed oxide films on the surface of the specimens, the nanoscratching technique was used.

In the process of nanoscratching, vertical and tangential forces are involved in the deformation of surfaces. As the relationship between these two forces is not governed by the Coulomb law of friction, other influencing factors must also be considered. Bowden et al. [79] proposed that friction resulted from the sum of two components: (i) a physical component which is the adhesion force required to shear the contacting junctions for sliding to occur; and (ii) the mechanical component due to the plastic deformation of the contacting surface arising from the ploughing. According to the Hertzian elastic contact theory [80] and the Bowden et al. [79] model of adhesive friction force, the adhesive friction coefficient becomes:

$$\mu_a = \tau_s \,.\, \pi \,.\left(\frac{3r}{4E_r}\right)^{\frac{2}{3}} .\, F_n^{\frac{-1}{3}} \tag{1}$$

where r is the tip radius, E_r the reduced modulus F_n the normal force and τ_s the interfacial shear strength [79]. Bowden et al [79] as well as Goddard et al. [81] proposed expressions for the ploughing friction coefficient. However, both expressions assumed that the contact area is a half disc, and their expressions were not corrected for elastic-plastic or viscoelastic contact [82–85]. Subsequently, Lafaye et al. [86] incorporate into the Goddard et al. [81] expression a term, which takes into account elastic recovery, assuming a real tip that is conical and truncated by a spherical cap at the extremity. Therefore, the equation, which allows to evaluate the ploughing friction coefficient is:

$$\mu_p = \frac{2}{a^2}\,\frac{\beta^2\, sin^{-1}\left(\frac{a\cos w}{\beta}\right) - a\cos w\,\sqrt{r^2 - a^2}}{\pi + 2w + \sin 2w} \tag{2}$$

where h the scratch depth and H the specimen hardness. The contact radius a, a fictive radius of the tip β and the angle made by the contact at the back of the sliding tip ω were calculated according to the geometrical expressions of [87,88].

$$\begin{cases} a = \sqrt{2hr - h^2} \\ \beta = \sqrt{r^2 - a^2 \sin^2 w} \\ w = \sin^{-1} \sqrt{\dfrac{2H(r-h)}{aE_r}} \end{cases} \tag{3}$$

The nanoscratch topography and cross section profile of the specimens are respectively shown in Figure 9. Higher penetration depths were achieved on the unreinforced specimens. Also, minimal, but noticeable variations in depths resulted from the scanning strategy and its respective process parameters (compare: Figure 9a against Figure 9b and Figure 9c against Figure 9d). The scratch cross section profile of the composite specimens is v-shaped perfectly symmetrical mirroring the profile of the tip. In conjunction with their lower penetration depths, this suggests that the existing films are possibly of low plasticity. Differently, the seen apparent smaller widths and the convex walls from the depth cross section profile of the unreinforced specimens are evidences of elastic recovery (occurring behind the scratch-tip) on the films.

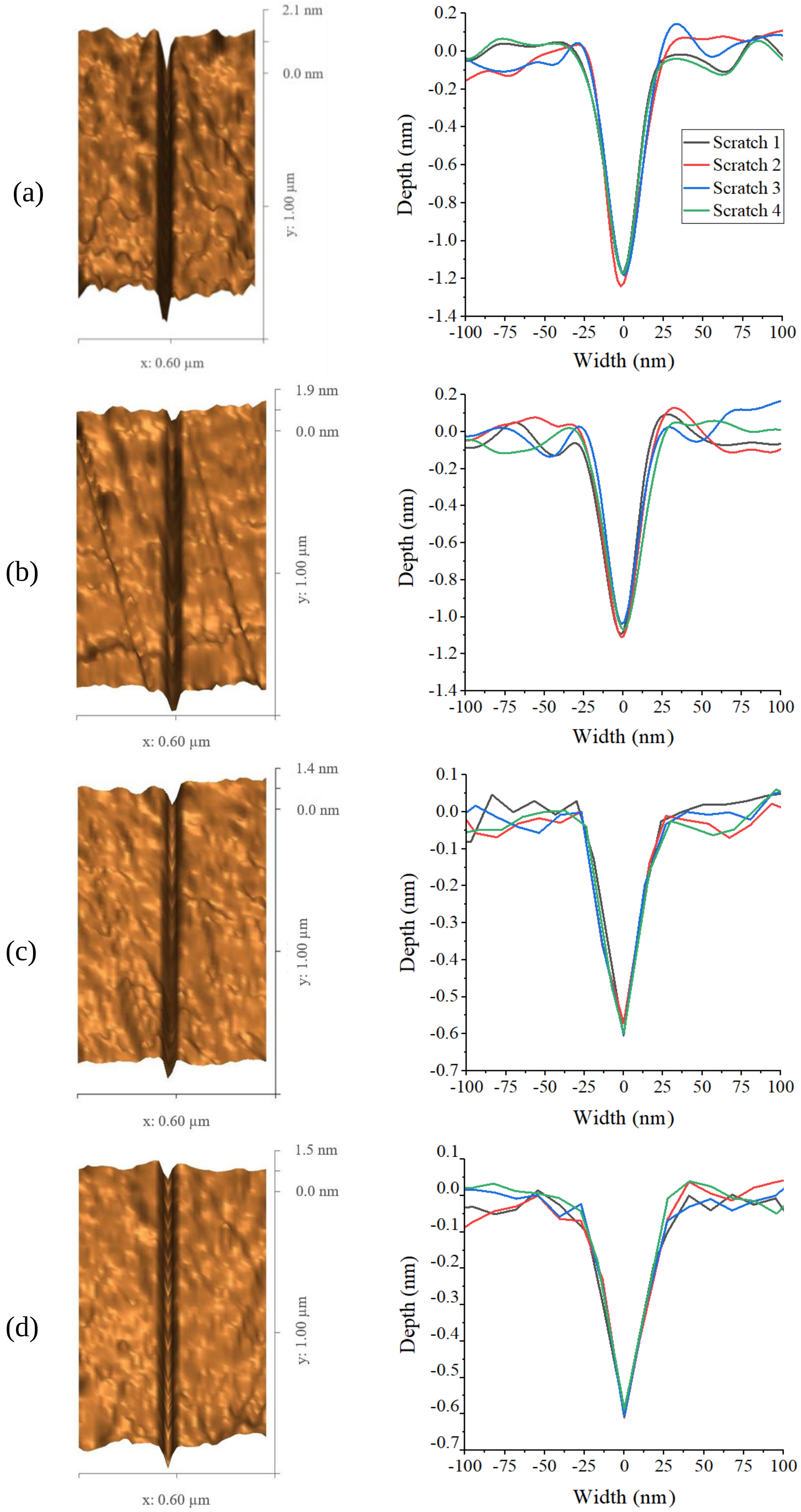

Figure 9 Atomic force microscopy scratches and the scratches cross section profiles of the specimen (a) 316L stripe hatching, (b) 316L sinusoidal hatching, (c) 316L-SiC stripe hatching and (d) 316L-SiC sinusoidal hatching.

The friction coefficient and specific wear rate of the specimens (wear volume per unit applied normal force per unit scratching distance) obtained from the nanoscratched surfaces are listed in Table 2. It is of interest to note the interrelationship of friction with wear. Specially, the disparities in friction coefficient and specific wear rate between the unreinforced and reinforced specimens. Which suggests that their films differ in physical and mechanical properties as well as chemistry. It is well known that 316L is a high corrosion resistant alloy due to its naturally formed protective passive film. Species of Fe (i.e. FeO_2 and Fe_3O_4), Cr (i.e. Cr_2O_3 and CrO_2), Mo (i.e. MoO_2 and MoO_3) and Ni (i.e. $Ni(OH)_2$ and NiO_2) formed from reactions with intrinsic elements (i.e. O, H, C, N), other metallic elements and impurities (i.e. sulphides and phosphides) are typically found within oxide films [89–96]. In fact, an oxide film formed on the surface of 316L can be composed of three layers: an inner layer of metallic Nickel at trace amount (if present), an intermediate layer of Fe species (existence of Cr species is also possible) and an outer layer of Fe and Mo species [96–100]. Unfortunately, if the oxide film exceeds a critical thickness, it can act as an abrasive during its contact with other surfaces, but if the thickness is less than a critical limit, then the oxide acts as a protective tribological film [101,102]. Additionally, when the hardness of the oxide is close to that of the bulk material and the oxide film thickness is of the order of 10 nm, the film will adhere well to the surface below and hence acts as a solid lubricant [103]. However, oxide films are susceptible to fretting as mechanical friction may destroy them more rapidly than they can grow [104,105], therefore introducing depassivation which will have a direct impact on corrosion, wear and friction.

Table 2 Nanoscratch friction coefficient and specific wear rate of the specimens. The data bounds noted are 95% confidence intervals.

Specimen	**Friction Coefficient**	**Specific Wear Rate x10^{-12} (m^3/N.m)**
316L stripe hatching	$0.239_{\pm 0.0074}$	$30.28_{\pm 0.85}$
316L sinusoidal hatching	$0.224_{\pm 0.0084}$	$26.35_{\pm 0.81}$
316L-SiC stripe hatching	$0.149_{\pm 0.0063}$	$15.39_{\pm 0.71}$
316L-SiC sinusoidal hatching	$0.150_{\pm 0.0064}$	$16.49_{\pm 0.53}$

To gain further understanding on the formed oxide films, deconvolution of their mechanical properties were investigated via in-situ nanoindentation. Graphs illustrating the evolution of nanohardness and reduced modulus within the oxide films are available in Appendix A. At 2 nm depth into the oxide films, both the nanohardness and reduced modulus were found to be much higher in the composites than in the unreinforced specimens. Also, it is worth noting that at this depth the nanohardness follows an expected trend reflecting on the specific wear rate values of Table 2. The depth into the oxide film which the nanohardness was closely related to the intrinsic nanohardness of the bulk material was: 20 nm for the 316L sinusoidal hatching, 30 nm for the 316L stripe hatching and 70 nm for the composite specimens. Therefore, this suggests the existence of a thicker oxide film on the composite specimens. Here, both the nanohardness and the reduced modulus of the films increased with the growing indentation depth. In fact, such a trend is characteristic of many oxides [106–108]. Since a more in-depth investigation is beyond the scope of this study, it can be speculated that discrepancies among the reported properties of oxide films are reasonably explained by the various growth environments.

3.6 Crystallography

The crystalline phase composition present in the specimens was evaluated by means of x-ray diffraction. Figure 10 confirms a fully austenitic structure on the 316L specimen printed using the stripe hatching. Apparently, the sinusoidal hatching led to a different heating and cooling rate in the meltpool, which failed to fully prevent the suppression of solute redistribution and resulted in a portion of the austenitic phase transforming into Fe_2Si and CrSi as confirmed by the JCPDS cards 83-1259 and 65-3298. An evident diffraction peak of SiC was observed in the composites spectrum and confirmed by the JCPDS card 89-1396. The presence of SiC in the microstructure suggests that complete dissolution of SiC particles was avoided under the used set of processing parameters and inherent rapid cooling rates of L-PBF. However, at a temperature of 883 K decomposition of SiC into Si and C atoms began, and according to the Fe-Si binary phase diagram, the phase transformation temperature decrease with increasing content of Si [30,109,110]. Therefore, Si atoms could have diffused into the lattice of molten Fe and consequently de-stabilise the austenite. In this regard, it is clear that displaced Si from SiC reacted with the matrix and contributed to the precipitation of silicide phases.

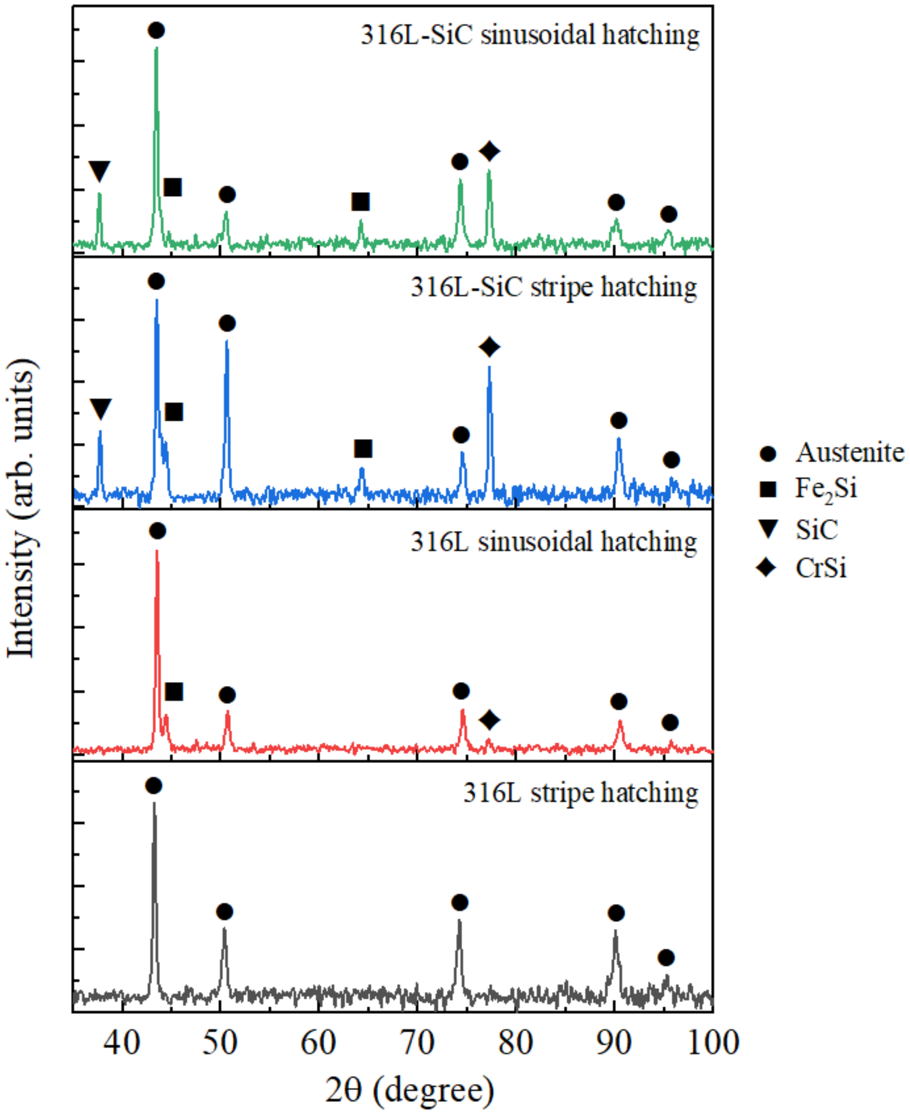

Figure 10 X-ray diffraction patterns of the printed specimens.

Electron backscatter diffraction grain orientation maps normal to the build direction and corresponding discrete pole figures of the austenitic phase are presented in Figure 11. It is observed that the specimens printed in this study are characterised by different crystallographic texture. A moderate {100} and {111} texture with preferable [101] and [001] grain growth was revealed in the pristine (unreinforced) 316L stripe hatching. In contrast, both composite specimens showed similar but a less strong texture, spread rather towards the {100} crystallographic family of planes. Nevertheless, the 316L-SiC sinusoidal hatching specimen presented a distinct fraction of [001] oriented grains. SiC and precipitated silicide phases had a weak contribution to the specimen's crystallographic texture. It was observed for SiC and CrSi a texture incline to the {100} pole, especially for SiC with orientation parallel to the hatching direction. In both printed composites, it is also observed that SiC grains were preferably oriented between [001] and [101]. On the other hand, grains of Fe$_2$Si were predominantly [210] and [120] oriented in the specimen 316L sinusoidal hatching, while the Fe$_2$Si phase present in the composites showed no clear contribution to texture. Supplementary pole figures are available in Figure B1 of Appendix B.

The electron backscatter diffraction analysis also showed that the total contribution of silicide phases to each specimen (316L sinusoidal hatching, 316L-SiC stripe hatching and 316L-SiC sinusoidal hatching) was less than 1 % (from this, approximately ¼ being of CrSi). As expected, most of these precipitated silicides (Fe_2Si and CrSi) were distributed along the grain boundaries of the austenite phase. This is because at grain boundaries the concentration of vacancies tends to be high, thus permitting easy diffusion of atoms. Additionally, as grain boundaries are potent nucleation sites, precipitating particles may have removed sufficient solute from the adjacent matrix such that the region in the proximity of the grain boundary remained free of precipitates [111–113].

There is clear evidence that both the addition of SiC and the used sinusoidal hatching promoted grain refinement. Large austenite grains underwent approximately 10 µm reduction in response to the sinusoidal hatching, bringing the largest size down to 55 µm in the unreinforced specimen and down to 36 µm in the composite specimen. The sinusoidal hatching system also impacted on the size distribution range of the remaining grains, for example in the unreinforced specimens it was reduced from 1-43 µm to 2-27 µm range. The 316L-SiC sinusoidal hatching presented the most refined microstructure of the four specimens, and this is supported by its low average 20 µm grain size, narrower grain size distribution, and lower as well as more homogeneous area fraction grain size. Electron backscatter diffraction grain maps and grain size distribution plots are available in Figure B2 of Appendix B.

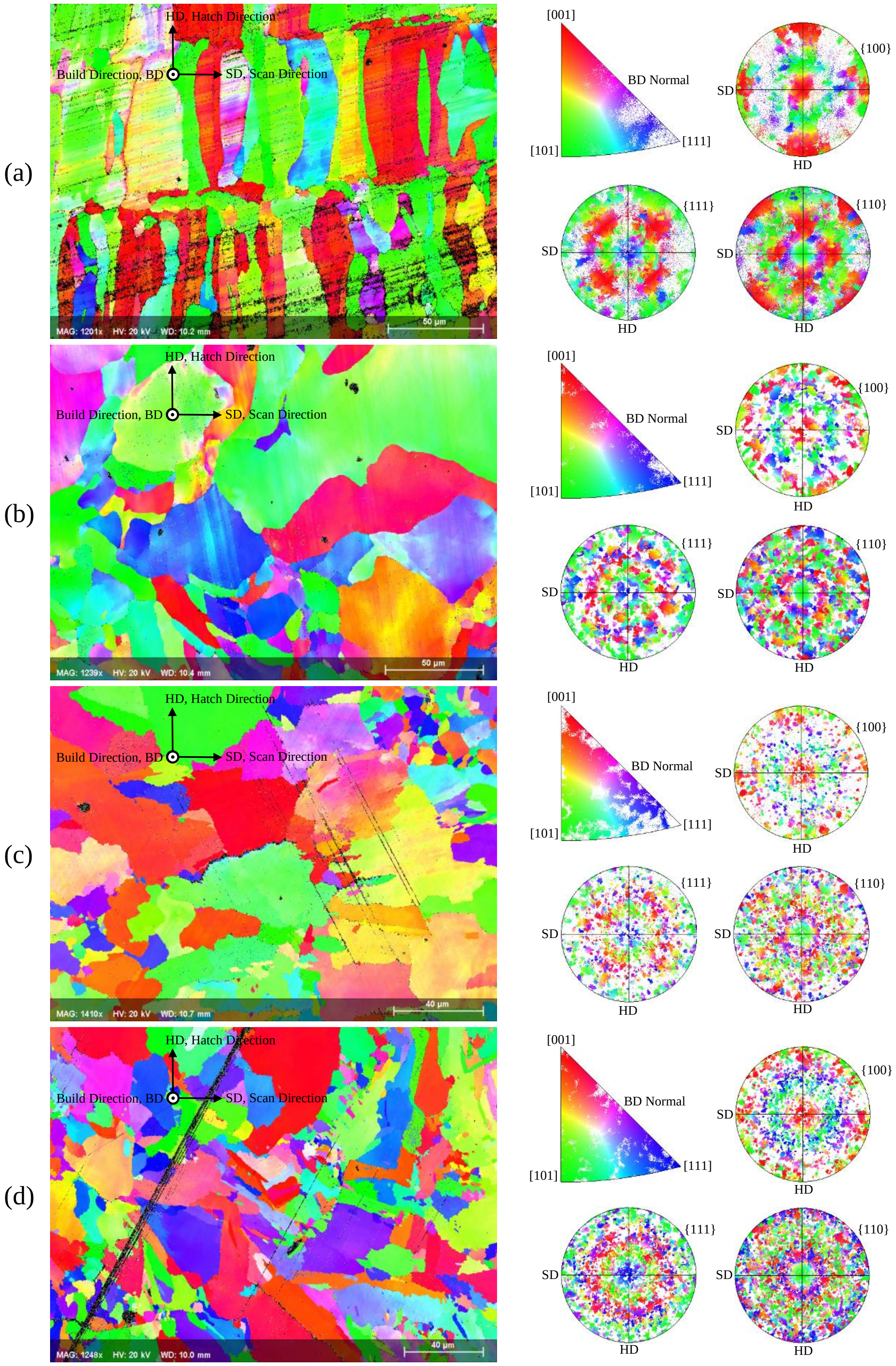

Figure 11 Electron backscatter diffraction discrete pole figures and inverse pole figures for (a) 316L stripe hatching, (b) 316L sinusoidal hatching, (c) 316L-SiC stripe hatching and (d) 316L-SiC sinusoidal hatching.

Journal of Materials Research and Technology
Volume 18, 2022, Pages 2672-2698
https://doi.org/10.1016/j.jmrt.2022.03.170

3.7 Chemical Analysis and Phase Mapping

Figure 12 illustrates secondary electron micrographs with corresponding overlaid energy dispersive x-ray spectroscopy mapping of silicon and carbon obtained from each of the specimens. Figure 12 also contrasts the electron backscatter diffraction phase map of the specimens. The observed elemental concentration increases from Figure 12a and 12b to Figure 12c and 12d is in agreement with the incorporated 1 wt.% SiC. The dispersion of silicon and carbon in the unreinforced specimens was apparently uniform, whereas in the reinforced specimens several carbon alignments were observed. The obtained electron backscatter diffraction phase constitution agrees with the x-ray diffraction results of Figure 10. However, as illustrated in Figure 12, SiC is the dominant reinforcing phase in the printed composites. Similarly to conventionally manufactured 316L-SiC composites [47,114], the composite printed with the stripe hatching system exhibited the aggregation of SiC grains, see the phase map in Figure 12c. On the other hand, the sinusoidal hatching system avoided the formation of large aggregates and showed an improved SiC dispersion in the 316L matrix. The impact of this can be related to the observed lesser microstructural cracking defects (Figure 8d) and overall refined microstructure (Figure B1d) when compared to the 316L-SiC stripe hatched specimen.

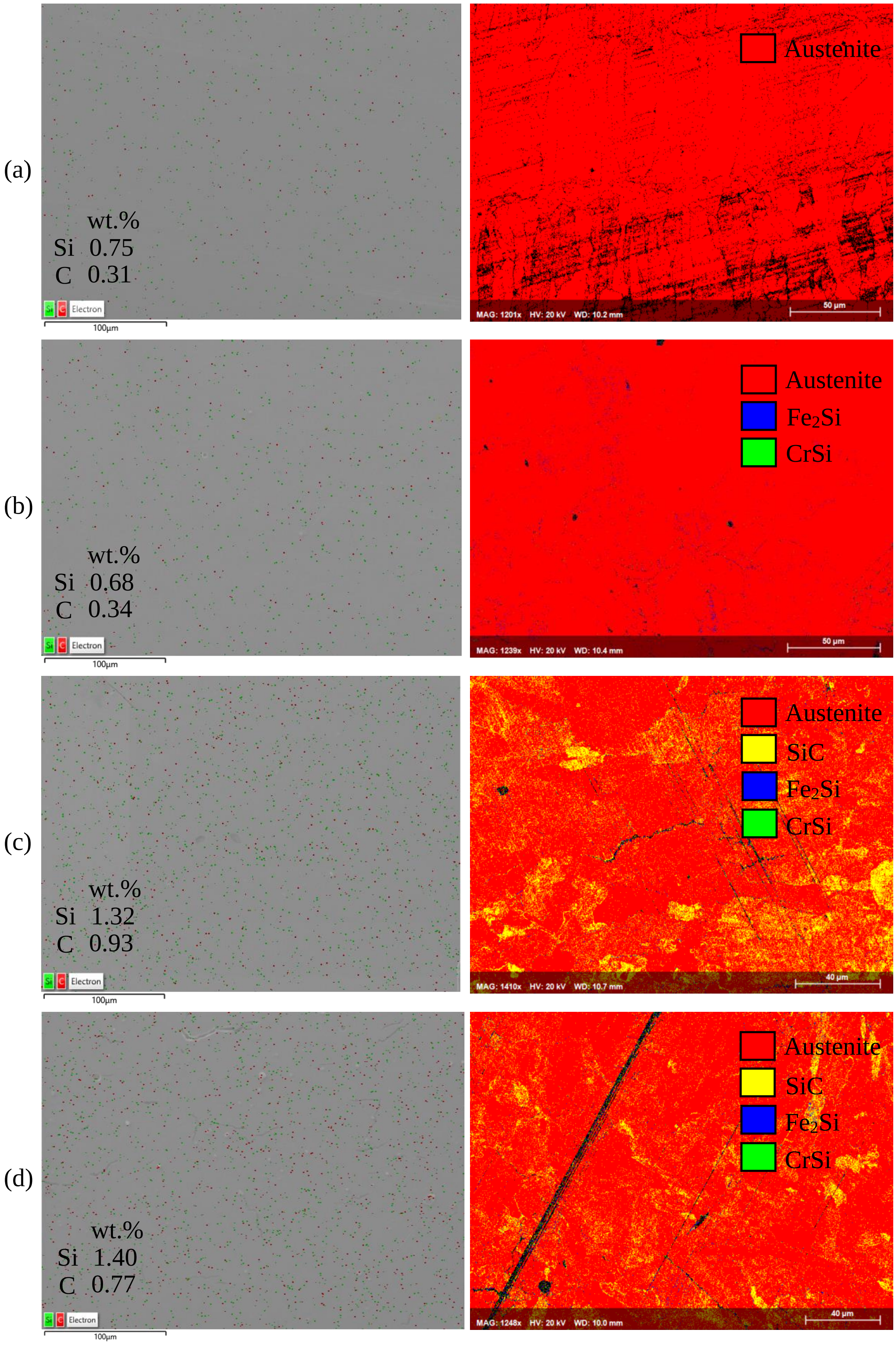

Figure 12 Energy dispersive spectroscopy analyses and electron backscatter diffraction phase map of (a) 316L stripe hatching, (b) 316L sinusoidal hatching, (c) 316L-SiC stripe hatching and (d) 316L-SiC sinusoidal hatching.

4. Discussion

4.1 Physical and Mechanical Properties of the Specimens

According to the density results, all the specimens possessed a relative low density. Yet, microstructural micrographs showed no evidence of lack of fusion defects, but there is a likelihood that lack of fusion defects could be present at other cross-section depths than those analysed. On the other hand, the micrographs do reveal the existence of severe porosity (pores smaller than 5 µm in diameter) within the specimen's microstructure, and these were located specially at grain boundaries. In this case, its typically said that the presence of moisture and entrapped gas from the feedstock powder, inappropriate shielding gas flow rate/velocity and excessive turbulence in the meltpool are the frequent causes of porosity [115–118]. However, it is most likely that instead, also supported by the observed spattering from the meltpools, a high energy input was used [119,120]. Therefore, the melting mechanism was dominated by either a transition or keyhole mode. The keyhole mode represents a highly unstable regime due to typical local temporal fluctuations of evaporation and flow imbalances along the wall of the keyhole cavity [121]. Therefore, it has a large potential of forming small gas bubbles that can get trapped within their meltpool during its rapid solidification. Nevertheless, the keyhole instability can be controlled [122–125]. The reason for this study not using the conductive mode of melting was linked to its productivity limitations, and in fact the keyhole mode is much more appreciated by the industry [126].

It is well known that lesser porosity and higher densification are prerequisites for obtaining greater hardness [127,128]. Despite their density and porosity, specimens printed in this study showed outstanding hardness. It is therefore clear that addressing these two issues additional hardness improvements are possible. A more detrimental impact of porosity was evidenced from the tensile results. As pores, crack initiation sites, drove the specimens to a premature failure in addition to affecting the yield and tensile strength attributed to loss of resistance area resulting from the presence of pores. During solidification, molted metal shrinks due to thermal contraction and in L-PBF this is impeded by the previously solidified layers underneath, which then forms strong compressive stresses at the interface layer. Similarly, the cyclic thermal stress could result in crack in response to residual stress release. Yet, the inherited residual stresses were not sufficient for generating cracks at the unreinforced specimens due to the high toughness and ductility of the 316L alloy. While in the composite specimens, the coefficient of thermal expansion mismatch between the SiC and 316L let to the generation of thermal stress in the SiC phase, and along with the accumulated residual stresses, this was the driving force of crack formation. Here, crack propagation followed the networks of grain boundaries, which resistance was weakened by the presence of pores and silicides. In the printing of composites with high scanning speeds such as that used for the sinusoidal hatching system, very high heating and cooling rates exists. Even though cracks were present in the composites printed with both low and high scanning speeds, it could be expected that the high scanning speed would introduce higher thermal shock and stress, which would then promote and accelerate crack initiation and propagation. However, this was not confirmed in this study. Here, a promising solution for inhibiting the initiation and propagation of crack is to attain further grain refinement to increase the microstructural barriers. Additionally, the preheating (at an optimal temperature) of the build substrate could retard the temperature gradient and cooling rates and reduce the magnitude of shrinkage stress. Therefore, this could be an effective mean of mitigating residual stress and solidification cracking.

4.2 Strengthening Mechanisms

The presented results demonstrated that superior mechanical properties were obtained from the SiC reinforced 316L composites. The enhanced strength can be explained by the role of nano SiC particulates, which activate multiple strengthening mechanisms. SiC particulates can be located both intergranularly and transgranularly within the 316L matrix. In the case of L-PBF 316L-SiC composites, several have reported the preferential distribution of SiC to grain boundaries [23,129,130], and this was assumed to be responsible for the inhibition of grain growth confirmed by Figure B2. Therefore, the composites strengthening can be explained by grain refinement according to the Hall-Petch effect and grain boundary strengthening. The addition of SiC to 316L also caused the precipitation of Fe_2Si and CrSi, and these precipitates are known for their strengthening effect [26,47,131]. The resulting precipitates confirmed the decomposition SiC into Si and C atoms. Therefore, the migration of C (and Si) into the austenitic matrix could possibly have taken place and so introduced solid solution strengthening effects. Additionally, partially the dispersed SiC nanoparticles could also have been retained and promoted heterogeneous nucleation during the solidification process, hence playing a role of dispersion strengthening. Therefore, the fine closely spaced hard SiC (and Fe_2Si and CrSi) particles at the austenite grain boundaries could account for dislocations pinning (Orowan strengthening [132,133]) and contribute to the strengthening of the 316L-SiC composites.

4.3 Tribological and Mechanical Properties of the Naturally Formed Oxide Films

In MMCs, understanding the nanotribology occurring at the interface of two contacting surfaces during their relative motion is necessary to develop fundamental understanding to many technological problems, including wear, friction and lubrication occurring at the nanoscale. Also, the importance of this is that it can lead to understanding tribology on the microscale. Adding up to the discussions accompanying the results, it is observed that despite having a much thicker oxide film, the composite specimens showed almost twofold reduction in friction coefficient and specific wear rate. In fact, the in-situ nanoindentation support these results with its reported nanohardness and reduced modulus. However, it should be noted that this is specifically for the 2 nm depth into the oxide film. The analysis made on the evolution of nanohardness and reduced modulus suggested that further into the oxide film, at a specific depth, different trend for friction and wear to that of Table 2 could exist. Ultimately, the influence of the naturally formed oxide films on the nanotribological response was quite different. Mechanically softer oxide layers exhibited an elastoplastic deformation behavior, eventually leading to higher wear. In contrast, harder and stiffer oxide layers led to a reduction in wear and friction. The broad implication of the presented study is that tuning the properties and characteristics of oxide films can therefore be beneficial for many applications to improve tribological performance.

4.4 Resulting Crystallographic Textures

Typically, the highest temperature gradient is located at the bottom of the meltpool and decreases nonlinearly towards the meltpool upper surface. Therefore, in response to the maximum heat flow, columnar grains grow predominantly parallel to the build direction. However, the results suggested that several grains also grew closely align with the hatching direction in the 316L stripe hatching specimen and in the remaining specimens rather closely aligned with the scanning direction. This is most likely consequential to the adopted keyhole mode of melting as high meltpool temperatures can lead to less aligned crystal growth with the build direction [134] due to the keyhole's meltpool promotion of multiple heat dissipating directions in response to the presence of irregular meltpool boundary morphologies. Therefore, the aforementioned along with the used processing parameters explain the absence of strong crystallographic textures.

The stripe hatching is the simplest and most commonly used hatching system in L-PBF. Additionally, several authors have reported it to develop strong <001> columnar grain alignments parallel to the build direction [61,135–138]. Instead, complex hatching systems such as islands [139–145] and fractals [38] have a more profound influence on grain morphologies and development of crystallographic textures. Accordingly, it was demonstrated in [63] [146] [147] that it is possible to control grain orientation as per hatching patterns. Therefore, this suggests that it is possible to grow grains with the sinusoidal hatching system which form sinusoidal patterns. With a such achievement, it would be interesting to verify the implications of sinusoidally oriented grains on the ductility of MMCs when applying tension along the hatching.

The existence of intragranular cellular structures in L-PBF 316L has been reported in a number of studies [148–157]. From these, it is worth noting that neighboring cellular colonies typically are misoriented with each other. As a matter of fact, the resulting misorientation obtained with the stripe hatching was consistent with these reports. However, the sinusoidal hatching system led to the development of cellular colonies highly oriented with the build direction. As contrasted in Figure 13, the rastering of the laser at 10000 mm/s along the sinusoidal path caused periodic oscillation of the molten along the scanning vector hence resulting in the solidification of short spaced overlapping dabs which influenced the orientation of cellular structures. In this respect, observations confirmed that the maximum temperature gradient controlling the cellular growth direction was vertically, and this being consistent between colonies. Reminding that a colony of cells is a group of cellular structures with the same morphological orientation and cell spacing.

One of the implications of having misoriented rather than highly oriented colonies of cellular structures is on the tensile performance of specimens. As shown by [157], tension perpendicular to the cells axis caused less deformation in response to accumulation of nano voids in the cellular microstructure, and additional stress then enlarged the nano void sizes breaking cellular boundaries. Under the same conditions, cells which tension was applied along their long axis were void free and the stress was relieved by cell deformation. In both scenarios, cells could only deform to a certain limit until the high tensile stress teared them apart. Therefore, based on these findings and as seen from the comparison of the tensile performance between the composites, the sinusoidal hatching can be used as a mean of collectively improving tensile strength and ductility. Additionally, the cellular microstructure resulting from the sinusoidal hatching could be used towards increasing composites toughness by deviating crack direction to longer paths. Even though both composites showed similar outstanding hardnesses, owing mainly to the barriers of dislocation motions imposed by cellular structures, it was observed that the 316L-SiC stripe hatching composite had a slightly higher hardness. Clearly, this is most likely to be related to the randomisation of the cellular colonies orientations which could potentially induce higher densities of entanglement dislocations. However, the colonies in the 316L-SiC sinusoidal hatching specimen were highly oriented and the reported hardness for this specimen was measured from the transversal axis of the cellular structures. This denotes that the hardness of this specimen with reference to the longitudinal axis of the cellular structures could be different.

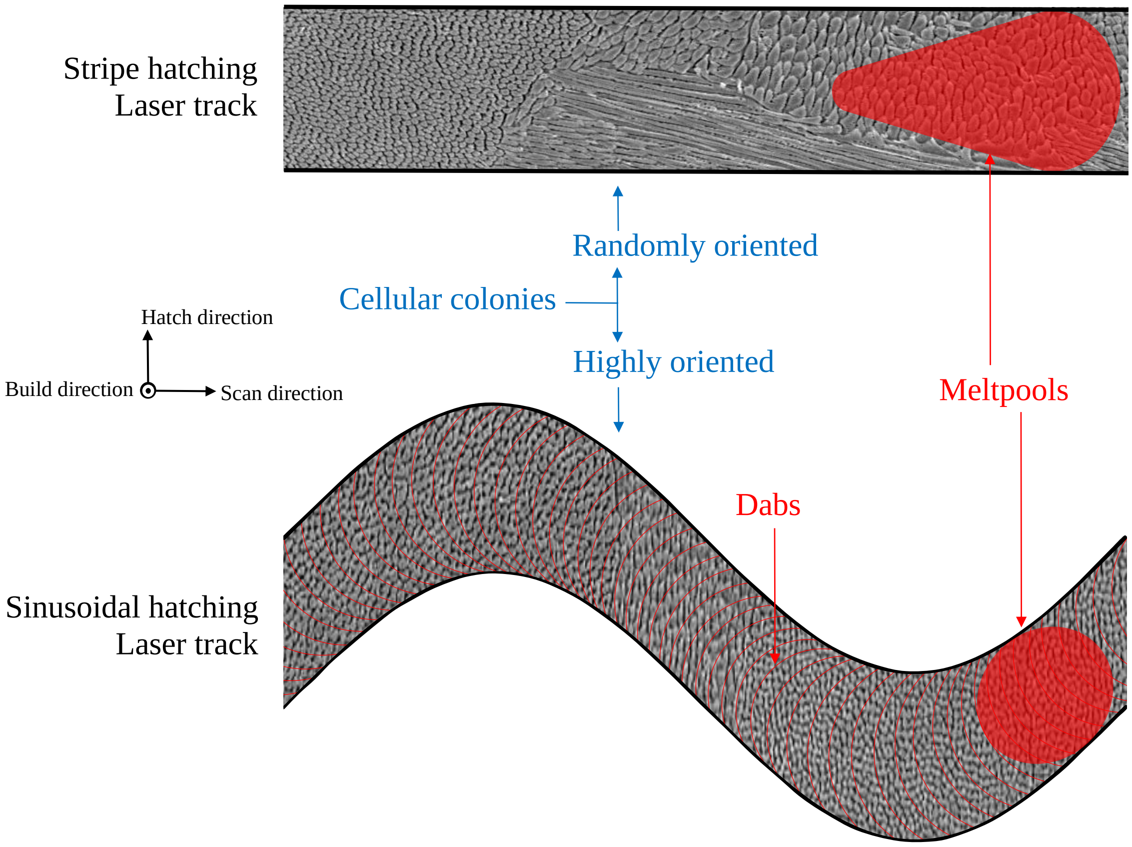

Figure 13 Schematic representation of the hatching systems and their resultant cellular structures.

4.5 Assessment of the Sinusoidal Hatching System

The sinusoidal hatching emerged as an important hatching system for L-PBF of MMCs. It proved to be capable of contributing to improvements in hardness, strength and ductility in composites. However, the existing gas porosity and solidification cracking within the composite microstructure prevented the exploitation of its full potential, therefore further research is recommended. Contrasting with the stripe hatching, over sixteenfold increase in scanning speed and over threefold reduction in laser power was successfully implemented in the sinusoidal hatching. Therefore, besides improving performance of composites, the sinusoidal hatching also helps to address the manufacturing lead time and process energy consumption issues concerning the L-PBF process [158,3].

The mechanisms which capacitated the sinusoidal hatching to promote suitable melting with such low laser power and extremely high scanning speed is speculated below. With the used scanning speed, the scanning of consecutive neighboring hatching paths was ultrafast. Therefore, the rate of heat flowing way from solidified zones because of argon flow convection and thermal radiation was reduced. Additionally, the sinusoidal profile of the laser paths is liked to have trapped pockets of hot argon and so reduced the efficiency of the gas flow as a cooling provider. Despite not using preheating, it was observed at the end of the printing job that the build substrate was approximately at 100 °C. Apparently, this temperature stabilised during the printing of the support structures in response to the argon flow and heat dissipation and transfer to the printer components. Therefore, it is clear that a much higher temperature than this in solidified neighboring hatching paths existed. In this respect, the stored thermal energy reflects well with the applied laser power. Another observation is the reduction of the meltpool width in contrast with the stripe hatching. Nonetheless, the width was very consistent along the sinusoidal paths and in fact it was found no clear evidence of lack of fusion defects.

5 Conclusions

A novel hatching strategy here named sinusoidal hatching was developed for L-PBF of MMCs. The presented investigational results provide a deep understanding regarding the effect of the sinusoidal hatching on the microstructure and mechanical properties. Comparison with the conventional stripe hatched composite shows that an increase in yield strength and ductility can be achieved by implementing the sinusoidal hatching. The tensile properties of the composites were compromised by the existing porosities and cracks which caused premature fractures and failure under the tensile loads. Their existence was attributed to trapped gas bubbles resulting from an unstable keyhole mode of melting and thermal expansion mismatch between the matrix and reinforcement along with accumulated residual stresses. Fortunately, these defects were less detrimental to the hardness. Confirmed by the literature, both composites showed an outstanding hardness. Yet, a slightly higher hardness was measured from the stripe hatched composite which was attributed to the randomised directional growth of cellular structures.

Friction and wear properties of the naturally formed oxide films and deconvolution of their mechanical properties were also investigated in this study. At approximately 1 nm depth into the oxide film, the composites already presented low plasticity, in contrast, elastic recovery was evidenced in the matrix specimens. As a matter of fact, these were consistent with the films nanohardness and reduced modulus, which also correlate with the twofold reduction in friction coefficient and specific wear rate measured from the composites. However, the depth into the oxide film which the nanohardness was closely related to the intrinsic nanohardness of the bulk material was 70 nm for the composites and 20 nm and 30 nm for the unreinforced stripe and sinusoidal hatched specimens. Additionally, the evolution of nanohardness and reduced modulus showed that further into the oxide film, at a specific depth, different trend for friction and wear to that reported could exist. Ultimately, mechanically softer oxide layers exhibited an elastoplastic deformation behavior, eventually leading to higher wear. In contrast, harder and stiffer oxide layers led to a reduction in wear and friction. The broad implication of the presented study is that tuning the properties and characteristics of oxide films can therefore be beneficial for many applications in order to improve tribological performance.

The sinusoidal hatched composite exhibited a highly refined columnar microstructure having a moderate {100} texture as most of the grains solidified preferentially in the <001> direction with respect to the build direction. A unique molten flow and solidification condition was stablished by the sinusoidal hatching. As periodic oscillation of the molten along the scanning vector resulted in the solidification of short spaced overlapping dabs which formed small colonies of intragranular cellular structures with cells highly oriented with the build direction. The implications of this reflected on the obtained improvements in yield strength and ductility seen from the sinusoidal hatched composite. It was speculated that, apart from tailoring hardness, the sinusoidal hatching could be used towards increasing composites toughness by deviating crack direction to longer paths. Besides improving composite performance, the sinusoidal hatching also reduced manufacturing lead time and process energy consumption.

The bulk mechanical properties of the composites were negatively affected by the existing porosities and cracks. Future research should therefore identify the source of theses defects and apply mitigation measures to eradicate them from the composite's microstructure. In-situ process monitoring of temperature and melt flow as well as build substrate preheating for mitigation of crack formation and residual stress are recommended.

The current study helps to pave the path towards addressing several endemic issues concerning mechanical performance and cost effectiveness of MMCs. As there is an increasing demand for materials with supernormal performance, the sinusoidal hatching is worth further research.

Acknowledgments

This publication has emanated from research supported by a research grant from Science Foundation Ireland (SFI) under Grant Number 16/RC/3872 and is co-funded under the European Regional Development Fund.

Scanning electron microscopy, atomic force macroscopy and nanoindentation were carried out at the Nano Research Facility in Dublin City University which was funded under the Programme for Research in Third Level Institutions (PRTLI) Cycle 5. The PRTLI is co-funded through the European Regional Development Fund (ERDF), part of the European Union Structural Funds Programme 2011-2015. Electron backscatter diffraction analysis was carried out at the Advanced Microscopy Laboratory in Trinity College Dublin. The authors are grateful for all the valuable technical support received from the staff members of these facilities.

Appendix A

Nanoindentation on the oxide film of the specimens was performed to support the nanoscratch study, and to measure the depth into the oxide film which the nanohardness is closely related to the nanohardness of the bulk material. The existence of surface defects, grain boundaries and phases affect the oxide film physical characteristics and chemistry. Here, each presented result is the average of six indents (2x3 matrix, 30µm spacing) obtained for the applied nanoindentation experimental design. The tip (a Berkovich diamond indenter) geometry and radius was calibrated with a fused quartz standard of known properties by running a series of tests that spans the load range of the instrument for area function determination and establishment of the compliance correction factor, both to be later utilised by the instrument software. Then, in-situ indentation mode of operation was chosen as it offered drift compensation capabilities for maximum accuracy. Prior performing each indent, a drift settle time of 300 s was applied while the tip waited on the specimen's surface in feedback prior to begin the drift correction procedure. This was to enable time for the motors and piezos to settle down. Then, the indentation procedures only began when the overall drift rate including thermal drift was within ±0.05 nm/s. All indentations were performed at room temperature. Figure A1 shows the evolution of the nanohardness within the oxide film and Figure A2 shows the evolution of the reduced modulus within the oxide film. The nanoindentation load-unload behavior of the 2, 10, 20, 30, 40, 50, 60, 70 nm depths into the oxide film is illustrated in Figure A3 and Figure A4.

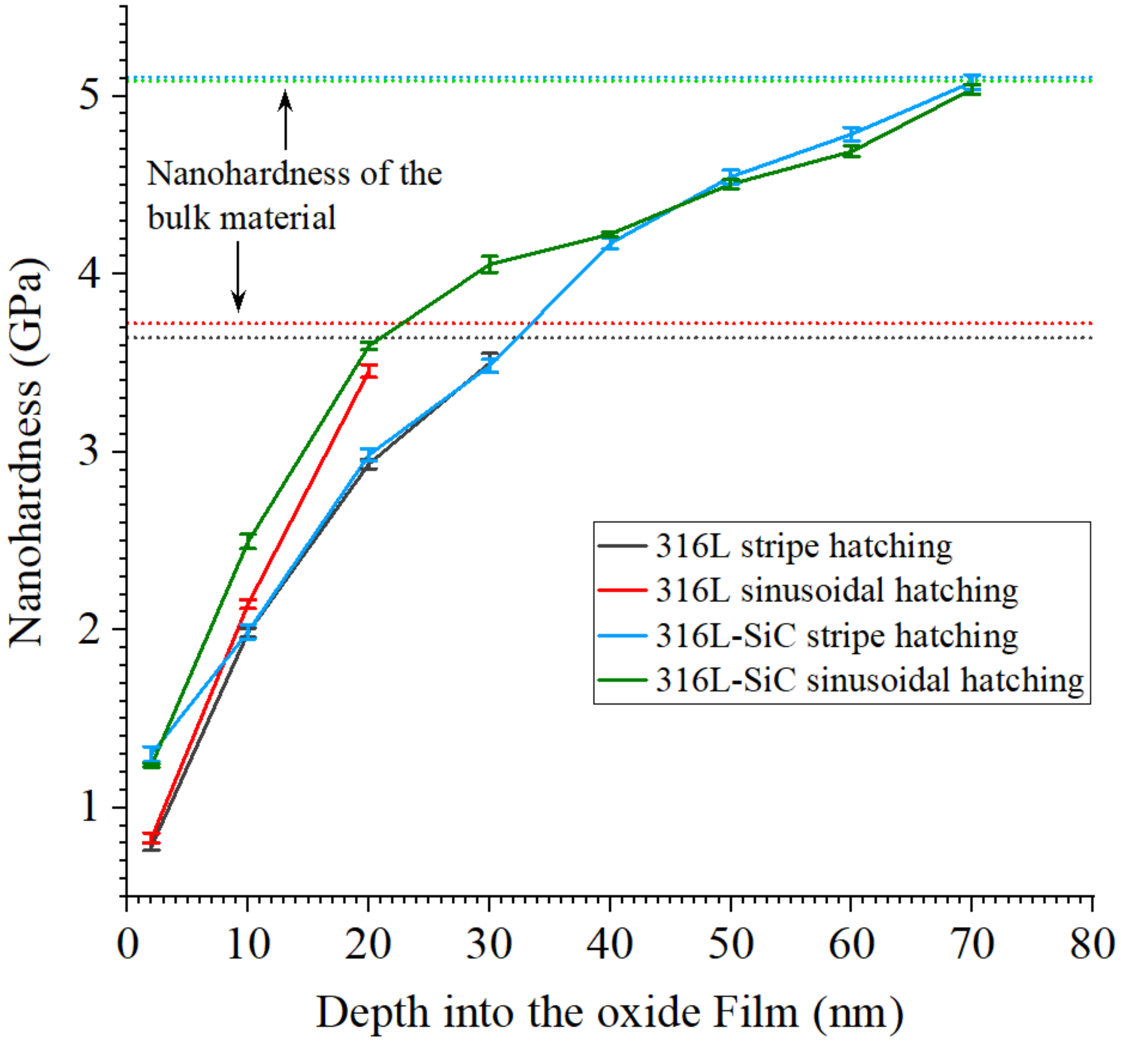

Figure A1 Evolution of the nanohardness within the oxide film. The data whiskers represent the 95% confidence interval.

Journal of Materials Research and Technology
Volume 18, 2022, Pages 2672-2698
https://doi.org/10.1016/j.jmrt.2022.03.170

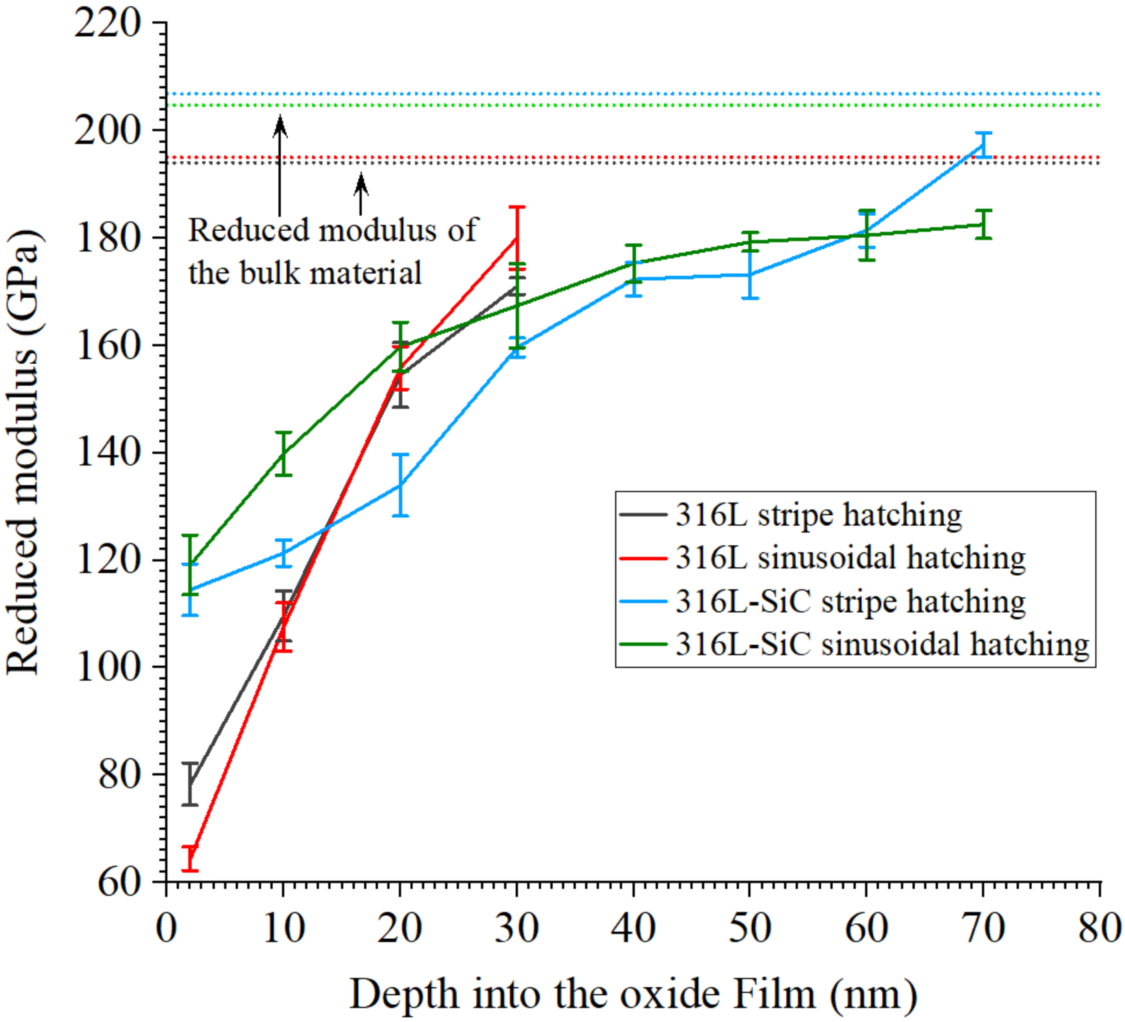

Figure A2 Evolution of the reduced modulus within the oxide film. The data whiskers represent the 95% confidence interval.

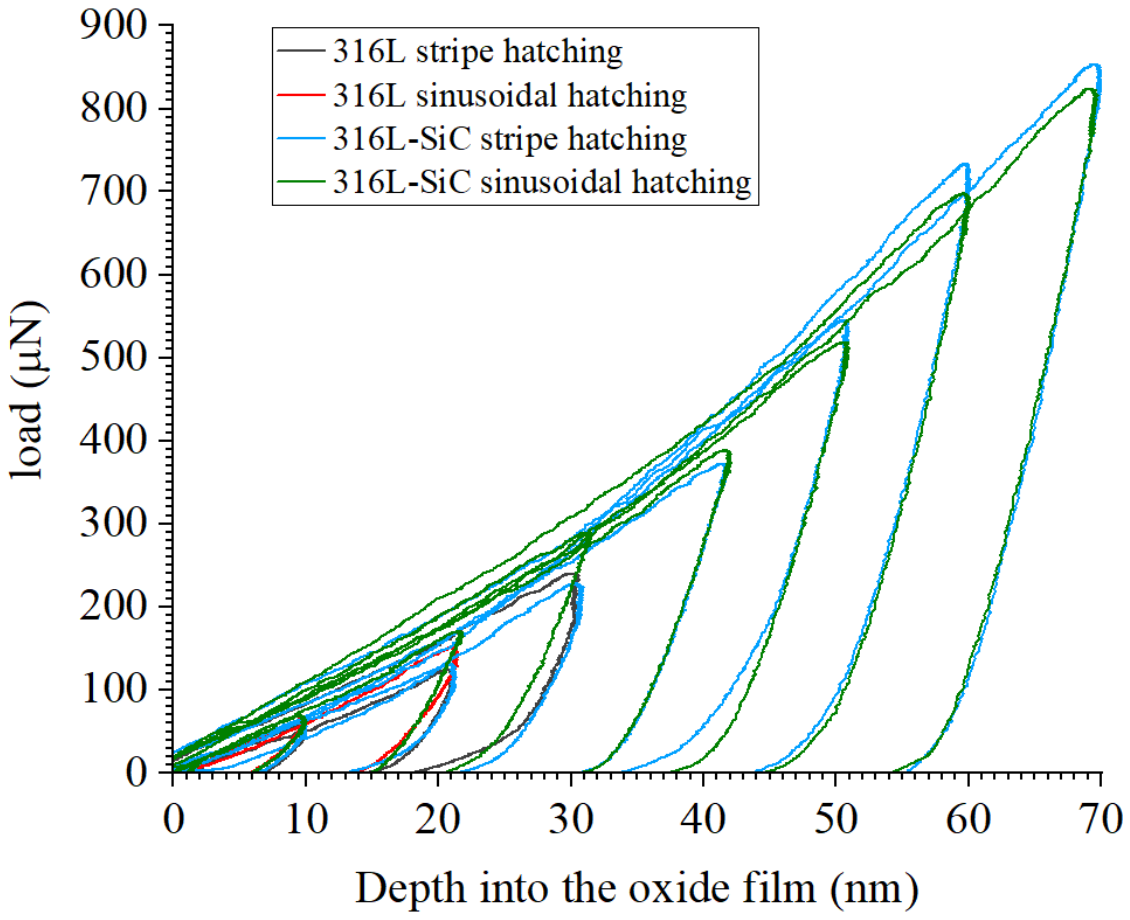

Figure A3 Nanoindentation load-unload behaviour of the 2, 10, 20, 30, 40, 50, 60, 70 nm depths into the oxide film.

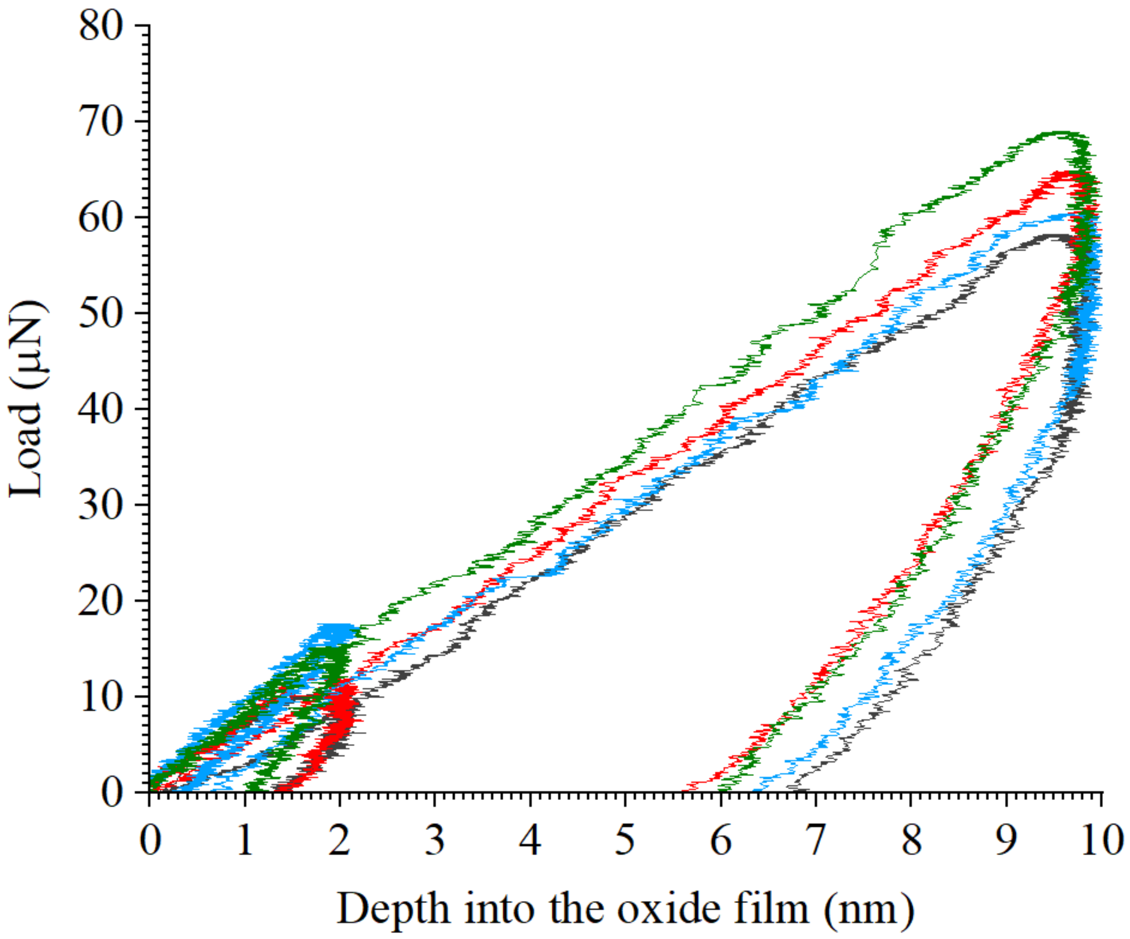

Figure A4 Supporting plot for Figure A3.

Appendix B

Inverse pole figures and pole figures of the precipitated silicides (Fe_2Si and CrSi) and SiC phase are available in Figure B1.

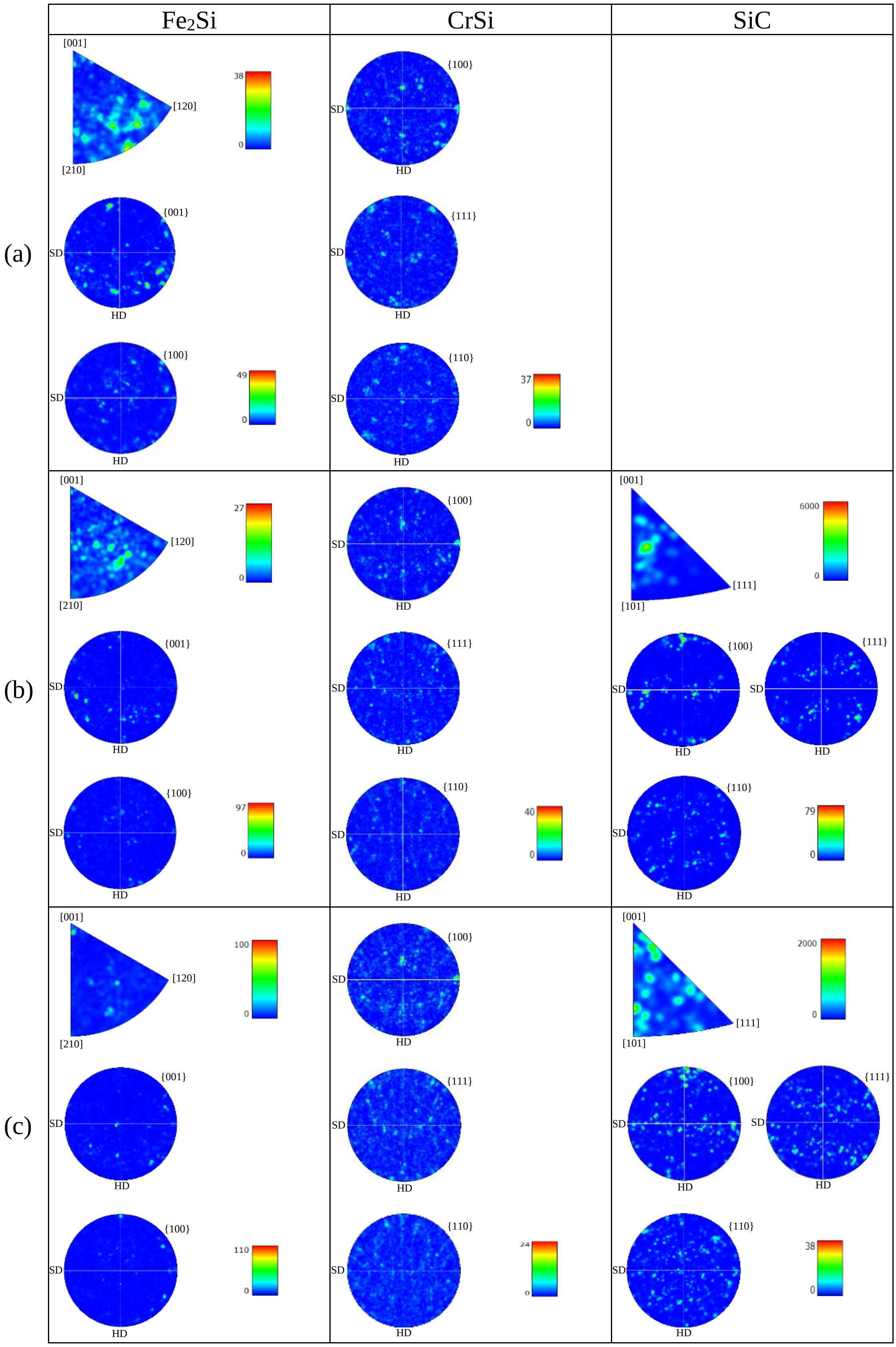

Figure B1 Additional electron backscatter diffraction build direction inverse pole figures and pole figures for (a) 316L sinusoidal hatching, (b) 316L-SiC stripe hatching and (c) 316L-SiC sinusoidal hatching.

Electron backscatter diffraction grain map and grain size distribution plot for the printed specimens are given in Figure B2.

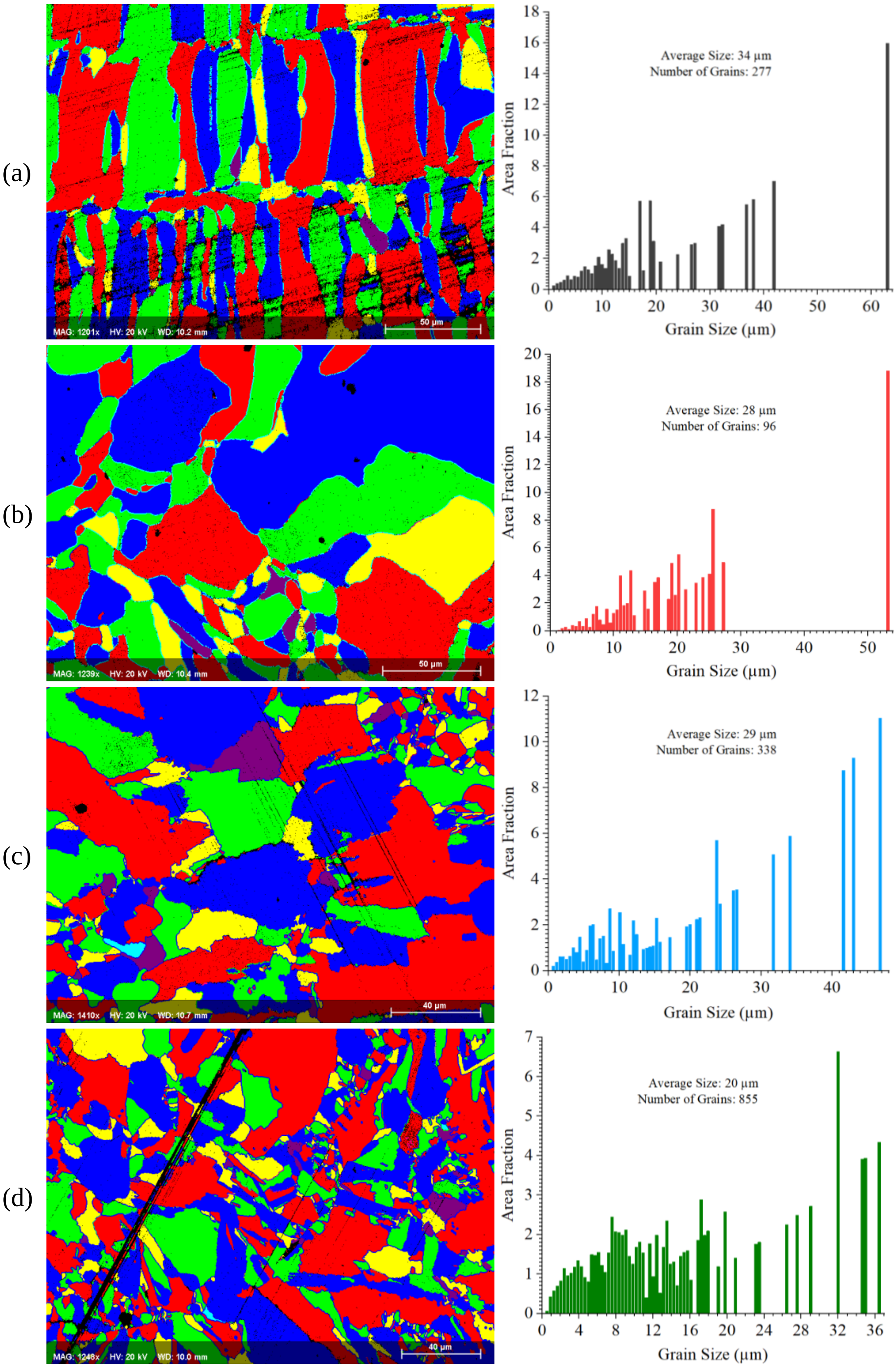

Figure B2 Electron backscatter diffraction grain map and grain size distribution plot for (a) 316L stripe hatching, (b) 316L sinusoidal hatching, (c) 316L-SiC stripe hatching and (d) 316L-SiC sinusoidal hatching.

Journal of Materials Research and Technology
Volume 18, 2022, Pages 2672-2698
https://doi.org/10.1016/j.jmrt.2022.03.170

References

[1] Cuevas, A. C., Becerril, E. B., Martínez, M. S., and Ruiz, J. L., 2018, *Metal Matrix Composites: Wetting and Infiltration*, Springer.

[2] Chand, S., and Chandrasekhar, P., 2020, "Influence of B4C/BN on Solid Particle Erosion of Al6061 Metal Matrix Hybrid Composites Fabricated through Powder Metallurgy Technique," Ceram. Int., **46**(11, Part A), pp. 17621–17630.

[3] Mussatto, A., Ahad, I. U., Mousavian, R. T., Delaure, Y., and Brabazon, D., 2021, "Advanced Production Routes for Metal Matrix Composites," Eng. Rep., **3**(5, e12330).

[4] Cantor, B., Dunne, F. P. E., and Stone, I. C., 2003, *Metal and Ceramic Matrix Composites*, CRC Press, Florida.

[5] Kim, J.-K., Tjong, S. C., and Mai, Y.-W., 2018, "4.2 Effect of Interface Strength on Metal Matrix Composites Properties," *Comprehensive Composite Materials II*, P.W.R. Beaumont, and C.H. Zweben, eds., Elsevier, Oxford, pp. 22–59.

[6] Prasad Behera, M., Dougherty, T., Singamneni, S., and De Silva, K., 2020, "Selective Laser Melting of Aluminium Metal-Matrix Composites and the Challenges," Mater. Today Proc., **33**, pp. 5729–5733.

[7] Han, T., Liu, E., Li, J., Zhao, N., and He, C., 2020, "A Bottom-up Strategy toward Metal Nano-Particles Modified Graphene Nanoplates for Fabricating Aluminum Matrix Composites and Interface Study," J. Mater. Sci. Technol., **46**, pp. 21–32.

[8] Han, T., Wang, F., Li, J., Zhao, N., and He, C., 2021, "Simultaneously Enhanced Strength and Ductility of Al Matrix Composites through the Introduction of Intragranular Nano-Sized Graphene Nanoplates," Compos. Part B Eng., **212**(108700).

[9] Behera, M. P., Dougherty, T., and Singamneni, S., 2019, "Conventional and Additive Manufacturing with Metal Matrix Composites: A Perspective," Procedia Manuf., **30**, pp. 159–166.

[10] Cepeda-Jiménez, C. M., and Pérez-Prado, M. T., 2018, "4.12 Processing of Nanoparticulate Metal Matrix Composites," *Comprehensive Composite Materials II*, P.W.R. Beaumont, and C.H. Zweben, eds., Elsevier, Oxford, pp. 313–330.

[11] Rajkumar, K., and Aravindan, S., 2013, "Tribological Behavior of Microwave Processed Copper–Nanographite Composites," Tribol. Int., **57**, pp. 282–296.

[12] Withers, P. J., and Clyne, T. W., eds., 1993, "The Interfacial Region," *An Introduction to Metal Matrix Composites*, Cambridge University Press, Cambridge, pp. 166–217.

[13] Yu, W. H., Sing, S. L., Chua, C. K., Kuo, C. N., and Tian, X. L., 2019, "Particle-Reinforced Metal Matrix Nanocomposites Fabricated by Selective Laser Melting: A State of the Art Review," Prog. Mater. Sci., **104**, pp. 330–379.

[14] Sahoo, B. P., and Das, D., 2019, "Critical Review on Liquid State Processing of Aluminium Based Metal Matrix Nano-Composites," Mater. Today Proc., **19**, pp. 493–500.

[15] Dasgupta, R., 2012, "Aluminium Alloy-Based Metal Matrix Composites: A Potential Material for Wear Resistant Applications," ISRN Metall., **2012**(e594573).

[16] Ashby, M. F., and Maine, E. M. A., 2000, "3.29 - Design Aspects of Metal Matrix Composite Usage," *Comprehensive Composite Materials*, A. Kelly, and C. Zweben, eds., Pergamon, Oxford, pp. 779–795.

[17] Zhao, X., Wei, Q. S., Gao, N., Zheng, E. L., Shi, Y. S., and Yang, S. F., 2019, "Rapid Fabrication of TiN/AISI 420 Stainless Steel Composite by Selective Laser Melting Additive Manufacturing," J. Mater. Process. Technol., **270**, pp. 8–19.

[18] Dadbakhsh, S., Mertens, R., Hao, L., Humbeeck, J. V., and Kruth, J.-P., 2019, “Selective Laser Melting to Manufacture ‘In Situ’ Metal Matrix Composites: A Review,” Adv. Eng. Mater., **21**(3).

[19] Jäcklein, M., Pfaff, A., and Hoschke, K., 2020, “Developing Tungsten-Filled Metal Matrix Composite Materials Using Laser Powder Bed Fusion,” Appl. Sci., **10**(24).

[20] Popov, V. V., Grilli, M. L., Koptyug, A., Jaworska, L., Katz-Demyanetz, A., Klobčar, D., Balos, S., Postolnyi, B. O., and Goel, S., 2021, “Powder Bed Fusion Additive Manufacturing Using Critical Raw Materials: A Review,” Materials, **14**(4).

[21] Kotadia, H. R., Gibbons, G., Das, A., and Howes, P. D., 2021, “A Review of Laser Powder Bed Fusion Additive Manufacturing of Aluminium Alloys: Microstructure and Properties,” Addit. Manuf., **46**.

[22] Bhuvanesh Kumar, M., and Sathiya, P., 2021, “Methods and Materials for Additive Manufacturing: A Critical Review on Advancements and Challenges,” Thin-Walled Struct., **159**.

[23] Zou, Y., Tan, C., Qiu, Z., Ma, W., Kuang, M., and Zeng, D., 2021, “Additively Manufactured SiC-Reinforced Stainless Steel with Excellent Strength and Wear Resistance,” Addit. Manuf., **41**.

[24] Wei, C., Chueh, Y.-H., Zhang, X., Huang, Y., Chen, Q., and Li, L., 2019, “Easy-To-Remove Composite Support Material and Procedure in Additive Manufacturing of Metallic Components Using Multiple Material Laser-Based Powder Bed Fusion,” J. Manuf. Sci. Eng., **141**(7).

[25] Song, B., Dong, S., and Coddet, C., 2014, “Rapid in Situ Fabrication of Fe/SiC Bulk Nanocomposites by Selective Laser Melting Directly from a Mixed Powder of Microsized Fe and SiC,” Scr. Mater., **75**, pp. 90–93.

[26] Dutta Majumdar, J., Kumar, A., and Li, L., 2009, “Direct Laser Cladding of SiC Dispersed AISI 316L Stainless Steel,” Tribol. Int., **42**(5), pp. 750–753.

[27] Wu, C. L., Zhang, S., Zhang, C. H., Zhang, J. B., Liu, Y., and Chen, J., 2019, “Effects of SiC Content on Phase Evolution and Corrosion Behavior of SiC-Reinforced 316L Stainless Steel Matrix Composites by Laser Melting Deposition,” Opt. Laser Technol., **115**, pp. 134–139.

[28] Pelleg, J., 1999, “Reactions in the Matrix and Interface of the Fe–SiC Metal Matrix Composite System,” Mater. Sci. Eng. A, **269**(1), pp. 225–241.

[29] Riquelme, A., Sánchez de Rojas Candela, C., Rodrigo, P., and Rams, J., 2022, “Influence of Process Parameters in Additive Manufacturing of Highly Reinforced 316L / SiCp Composites,” J. Mater. Process. Technol., **299**, p. 117325.

[30] Wu, C. L., Zhang, S., Zhang, C. H., Zhang, J. B., Liu, Y., and Chen, J., 2019, “Effects of SiC Content on Phase Evolution and Corrosion Behavior of SiC-Reinforced 316L Stainless Steel Matrix Composites by Laser Melting Deposition,” Opt. Laser Technol., **115**, pp. 134–139.

[31] Jia, H., Sun, H., Wang, H., Wu, Y., and Wang, H., 2021, “Scanning Strategy in Selective Laser Melting (SLM): A Review,” Int. J. Adv. Manuf. Technol., **113**(9), pp. 2413–2435.

[32] Zhang, W., Tong, M., and Harrison, N. M., 2020, “Scanning Strategies Effect on Temperature, Residual Stress and Deformation by Multi-Laser Beam Powder Bed Fusion Manufacturing,” Addit. Manuf., **36**.

[33] Serrano-Munoz, I., Mishurova, T., Thiede, T., Sprengel, M., Kromm, A., Nadammal, N., Nolze, G., Saliwan-Neumann, R., Evans, A., and Bruno, G., 2020, “The Residual Stress in As-Built Laser Powder Bed Fusion IN718 Alloy as a Consequence of the Scanning Strategy Induced Microstructure,” Sci. Rep., **10**(1).

[34] Cheng, B., Shrestha, S., and Chou, K., 2016, "Stress and Deformation Evaluations of Scanning Strategy Effect in Selective Laser Melting," Addit. Manuf., **12**, pp. 240–251.
[35] Obeidi, M. A., Monu, M., Hughes, C., Bourke, D., Dogu, M. N., Francis, J., Zhang, M., Ahad, I. U., and Brabazon, D., 2021, "Laser Beam Powder Bed Fusion of Nitinol Shape Memory Alloy (SMA)," J. Mater. Res. Technol., **14**, pp. 2554–2570.
[36] Jarfors, A. E. W., Shashidhar, A. C. G. H., Yepur, H. K., Steggo, J., Andersson, N.-E., and Stolt, R., 2021, "Build Strategy and Impact Strength of SLM Produced Maraging Steel (1.2709)," Metals, **11**(1), p. 51.
[37] Jiang, J., and Ma, Y., 2020, "Path Planning Strategies to Optimize Accuracy, Quality, Build Time and Material Use in Additive Manufacturing: A Review," Micromachines, **11**(7), p. 633.
[38] Catchpole-Smith, S., Aboulkhair, N., Parry, L., Tuck, C., Ashcroft, I. A., and Clare, A., 2017, "Fractal Scan Strategies for Selective Laser Melting of 'Unweldable' Nickel Superalloys," Addit. Manuf., **15**, pp. 113–122.
[39] Yang, J., Bin, H., Zhang, X., and Liu, Z., 2003, "Fractal Scanning Path Generation and Control System for Selective Laser Sintering (SLS)," Int. J. Mach. Tools Manuf., **43**(3), pp. 293–300.
[40] Bo, Q., Yu-sheng, S., Qing-song, W., and Hai-bo, W., 2012, "The Helix Scan Strategy Applied to the Selective Laser Melting," Int. J. Adv. Manuf. Technol., **63**(5), pp. 631–640.
[41] Yang, Y., Loh, H. T., Fuh, J. Y. H., and Wang, Y. G., 2002, "Equidistant Path Generation for Improving Scanning Efficiency in Layered Manufacturing," Rapid Prototyp. J., **8**(1), pp. 30–37.
[42] Ding, D., Pan, Z., Cuiuri, D., and Li, H., 2015, "A Practical Path Planning Methodology for Wire and Arc Additive Manufacturing of Thin-Walled Structures," Robot. Comput.-Integr. Manuf., **34**, pp. 8–19.
[43] Jafari, D., Vaneker, T. H. J., and Gibson, I., 2021, "Wire and Arc Additive Manufacturing: Opportunities and Challenges to Control the Quality and Accuracy of Manufactured Parts," Mater. Des., **202**.
[44] Ding, D., Pan, Z., Cuiuri, D., Li, H., and Larkin, N., 2016, "Adaptive Path Planning for Wire-Feed Additive Manufacturing Using Medial Axis Transformation," J. Clean. Prod., **133**, pp. 942–952.
[45] Zhao, D., and Guo, W., 2019, "Shape and Performance Controlled Advanced Design for Additive Manufacturing: A Review of Slicing and Path Planning," J. Manuf. Sci. Eng., **142**(1).
[46] Zhang, L., Ding, L., Ullah, S., Hu, T., Xu, Y., Chen, L., and Hanif, M., 2020, "An Improved Medial Axis Path Generation Algorithm for Selective Laser Melting," Rapid Prototyp. J., **26**(10), pp. 1751–1759.
[47] Mussatto, A., Groarke, R., A-Hameed, A., Ahad, I. U. I., Vijayaraghavan, R. K., O'Neill, A., McNally, P., Delaure, Y., and Brabazon, D., 2019, "Evaluation via Powder Metallurgy of Nano-Reinforced Iron Powders Developed for Selective Laser Melting Applications," Mater. Des., **182**.
[48] Mussatto, A., Groarke, R., O'Neill, A., Obeidi, M. A., Delaure, Y., and Brabazon, D., 2021, "Influences of Powder Morphology and Spreading Parameters on the Powder Bed Topography Uniformity in Powder Bed Fusion Metal Additive Manufacturing," Addit. Manuf., **38**.
[49] Mussatto, A., Groarke, R., Vijayaraghavan, R. K., Hughes, C., Obeidi, M. A., Doğu, M. N., Yalçin, M. A., McNally, P. J., Delaure, Y., and Brabazon, D., 2022,

"Assessing Dependency of Part Properties on the Printing Location in Laser-Powder Bed Fusion Metal Additive Manufacturing," Mater. Today Commun., **30**.

[50] ASTM E92, 2017, *Standard Test Methods for Vickers Hardness and Knoop Hardness of Metallic Materials,* West Conshohocken, PA.

[51] ASTM E8/E8M, 2009, *Standard Test Methods for Tension Testing of Metallic Materials*, ASTM International, West Conshohocken, PA.

[52] Mohr, G., Altenburg, S. J., and Hilgenberg, K., 2020, "Effects of Inter Layer Time and Build Height on Resulting Properties of 316L Stainless Steel Processed by Laser Powder Bed Fusion," Addit. Manuf., **32**.

[53] Leicht, A., Yu, C. H., Luzin, V., Klement, U., and Hryha, E., 2020, "Effect of Scan Rotation on the Microstructure Development and Mechanical Properties of 316L Parts Produced by Laser Powder Bed Fusion," Mater. Charact., **163**.

[54] Heiden, M. J., Deibler, L. A., Rodelas, J. M., Koepke, J. R., Tung, D. J., Saiz, D. J., and Jared, B. H., 2019, "Evolution of 316L Stainless Steel Feedstock Due to Laser Powder Bed Fusion Process," Addit. Manuf., **25**, pp. 84–103.

[55] Duval-Chaneac, M. S., Gao, N., Khan, R. H. U., Giles, M., Georgilas, K., Zhao, X., and Reed, P. A. S., 2021, "Fatigue Crack Growth in IN718/316L Multi-Materials Layered Structures Fabricated by Laser Powder Bed Fusion," Int. J. Fatigue, **152**, p. 106454.

[56] Ahmed, N., Barsoum, I., Haidemenopoulos, G., and Al-Rub, R. K. A., 2022, "Process Parameter Selection and Optimization of Laser Powder Bed Fusion for 316L Stainless Steel: A Review," J. Manuf. Process., **75**, pp. 415–434.

[57] Liang, A., Pey, K. S., Polcar, T., and Hamilton, A. R., 2022, "Effects of Rescanning Parameters on Densification and Microstructural Refinement of 316L Stainless Steel Fabricated by Laser Powder Bed Fusion," J. Mater. Process. Technol., **302**.

[58] Pineau, A., Benzerga, A. A., and Pardoen, T., 2016, "Failure of Metals I: Brittle and Ductile Fracture," Acta Mater., **107**, pp. 424–483.

[59] Bian, L., Shamsaei, N., and Usher, J. M., 2017, *Laser-Based Additive Manufacturing of Metal Parts: Modeling, Optimization, and Control of Mechanical Properties*, CRC Press, Florida.

[60] Barkia, B., Aubry, P., Haghi-Ashtiani, P., Auger, T., Gosmain, L., Schuster, F., and Maskrot, H., 2020, "On the Origin of the High Tensile Strength and Ductility of Additively Manufactured 316L Stainless Steel: Multiscale Investigation," J. Mater. Sci. Technol., **41**, pp. 209–218.

[61] Sun, Z., Tan, X., Tor, S. B., and Chua, C. K., 2018, "Simultaneously Enhanced Strength and Ductility for 3D-Printed Stainless Steel 316L by Selective Laser Melting," NPG Asia Mater., **10**(4), pp. 127–136.

[62] Sun, Z., Tan, X., Tor, S. B., and Yeong, W. Y., 2016, "Selective Laser Melting of Stainless Steel 316L with Low Porosity and High Build Rates," Mater. Des., **104**, pp. 197–204.

[63] Pham, M.-S., Dovgyy, B., Hooper, P. A., Gourlay, C. M., and Piglione, A., 2020, "The Role of Side-Branching in Microstructure Development in Laser Powder-Bed Fusion," Nat. Commun., **11**(1), p. 749.

[64] Gäumann, M., Henry, S., Cléton, F., Wagnière, J.-D., and Kurz, W., 1999, "Epitaxial Laser Metal Forming: Analysis of Microstructure Formation," Mater. Sci. Eng. A, **271**(1), pp. 232–241.

[65] Boettinger, W. J., Coriell, S. R., Greer, A. L., Karma, A., Kurz, W., Rappaz, M., and Trivedi, R., 2000, "Solidification Microstructures: Recent Developments, Future Directions," Acta Mater., **48**(1), pp. 43–70.

[66] Wu, C. S., Wang, L., Ren, W. J., and Zhang, X. Y., 2014, "Plasma Arc Welding: Process, Sensing, Control and Modeling," J. Manuf. Process., **16**(1), pp. 74–85.
[67] Chen, S. B., and Lv, N., 2014, "Research Evolution on Intelligentized Technologies for Arc Welding Process," J. Manuf. Process., **16**(1), pp. 109–122.
[68] Liskevych, O., and Scotti, A., 2015, "Influence of the CO2 Content on Operational Performance of Short-Circuit GMAW," Weld. World, **59**(2), pp. 217–224.
[69] Criss, E. M., Smith, R. J., and Meyers, M. A., 2015, "Failure Mechanisms in Cobalt Welded with a Silver–Copper Filler," Mater. Sci. Eng. A, **645**, pp. 369–382.
[70] Xu, H., Xu, L. D., Zhang, S. J., and Han, Q., 2006, "Effect of the Alloy Composition on the Grain Refinement of Aluminum Alloys," Scr. Mater., **54**(12), pp. 2191–2196.
[71] Fan, Z., Gao, F., Wang, Y., Men, H., and Zhou, L., 2021, "Effect of Solutes on Grain Refinement," Prog. Mater. Sci.
[72] Gupta, M., and Surappa, M. K., 1995, "Effect of Increase in Heterogeneous Nucleation Sites on the Aging Behavior of 6061/SiC Metal Matrix Composites," Mater. Res. Bull., **30**(8), pp. 1023–1030.
[73] Tosun, G., and Kurt, M., 2019, "The Porosity, Microstructure, and Hardness of Al-Mg Composites Reinforced with Micro Particle SiC/Al2O3 Produced Using Powder Metallurgy," Compos. Part B Eng., **174.**
[74] Galy, C., Le Guen, E., Lacoste, E., and Arvieu, C., 2018, "Main Defects Observed in Aluminum Alloy Parts Produced by SLM: From Causes to Consequences," Addit. Manuf., **22**, pp. 165–175.
[75] Wei, Q., Li, S., Han, C., Li, W., Cheng, L., Hao, L., and Shi, Y., 2015, "Selective Laser Melting of Stainless-Steel/Nano-Hydroxyapatite Composites for Medical Applications: Microstructure, Element Distribution, Crack and Mechanical Properties," J. Mater. Process. Technol., **222**, pp. 444–453.
[76] Evans, A., Marchi, C. S., and Mortensen, A., 2003, *Metal Matrix Composites in Industry: An Introduction and a Survey*, Springer, New York.
[77] Clyne, T. W., and Withers, P. J., 1993, *An Introduction to Metal Matrix Composites*, Cambridge University Press, Cambridge.
[78] Bhushan, B., 2013, *Introduction to Tribology*, John Wiley & Sons, New York.
[79] Bowden, F. P., Bowden, F. P., and Tabor, D., 2001, *The Friction and Lubrication of Solids*, Clarendon Press, Oxford.
[80] Johnson, K. L., 1987, *Contact Mechanics*, Cambridge University Press, Camdridge.
[81] Goddard, J., and Wilman, H., 1962, "A Theory of Friction and Wear during the Abrasion of Metals," Wear, **5**(2), pp. 114–135.
[82] Lafaye, S., Gauthier, C., and Schirrer, R., 2005, "A Surface Flow Line Model of a Scratching Tip: Apparent and True Local Friction Coefficients," Tribol. Int., **38**(2), pp. 113–127.
[83] Bucaille, J. L., Felder, E., and Hochstetter, G., 2001, "Mechanical Analysis of the Scratch Test on Elastic and Perfectly Plastic Materials with the Three-Dimensional Finite Element Modeling," Wear, **249**(5), pp. 422–432.
[84] Lafaye, S., Gauthier, C., and Schirrer, R., 2006, "Analysis of the Apparent Friction of Polymeric Surfaces," J. Mater. Sci., **41**(19), pp. 6441–6452.
[85] Gauthier, C., Lafaye, S., and Schirrer, R., 2001, "Elastic Recovery of a Scratch in a Polymeric Surface: Experiments and Analysis," Tribol. Int., **34**(7), pp. 469–479.

[86] Lafaye, S., Gauthier, C., and Schirrer, R., 2006, "The Ploughing Friction: Analytical Model with Elastic Recovery for a Conical Tip with a Blunted Spherical Extremity," Tribol. Lett., **21**(2), pp. 95–99.

[87] Lafaye, S., and Troyon, M., 2006, "On the Friction Behaviour in Nanoscratch Testing," Wear, **261**(7), pp. 905–913.

[88] Mishra, M., and Szlufarska, I., 2012, "Analytical Model for Plowing Friction at Nanoscale," Tribol. Lett., **45**(3), pp. 417–426.

[89] Yang, X., Tang, F., Hao, X., and Li, Z., 2021, "Oxide Evolution During the Solidification of 316L Stainless Steel from Additive Manufacturing Powders with Different Oxygen Contents," Metall. Mater. Trans. B, **52**(4), pp. 2253–2262.

[90] Harun, W. S. W., Asri, R. I. M., Romlay, F. R. M., Sharif, S., Jan, N. H. M., and Tsumori, F., 2018, "Surface Characterisation and Corrosion Behaviour of Oxide Layer for SLMed-316L Stainless Steel," J. Alloys Compd., **748**, pp. 1044–1052.

[91] Habib, K. A., Damra, M. S., Saura, J. J., Cervera, I., and Bellés, J., 2011, "Breakdown and Evolution of the Protective Oxide Scales of AISI 304 and AISI 316 Stainless Steels under High-Temperature Oxidation," Int. J. Corros., **2011**.

[92] Maurice, V., Yang, W. P., and Marcus, P., 1998, "X-Ray Photoelectron Spectroscopy and Scanning Tunneling Microscopy Study of Passive Films Formed on (100) Fe-18Cr-13Ni Single-Crystal Surfaces," J. Electrochem. Soc., **145**(3).

[93] Apell, J., Wonneberger, R., Seyring, M., Stöcker, H., Rettenmayr, M., and Undisz, A., 2021, "Early Oxidation Stages of a Co-Cr-Fe-Mn-Ni-Si Complex Concentrated Alloy with Cr, Mn, and Si Contents Matching Those of 316L Stainless Steel," Corros. Sci., **190**.

[94] Wang, Z., Paschalidou, E.-M., Seyeux, A., Zanna, S., Maurice, V., and Marcus, P., 2019, "Mechanisms of Cr and Mo Enrichments in the Passive Oxide Film on 316L Austenitic Stainless Steel," Front. Mater., **6**.

[95] Holcomb, G. R., Tylczak, J., and Carney, C., 2015, "Oxidation of CoCrFeMnNi High Entropy Alloys," JOM, **67**(10), pp. 2326–2339.

[96] Wang, Z., Di-Franco, F., Seyeux, A., Zanna, S., Maurice, V., and Marcus, P., 2019, "Passivation-Induced Physicochemical Alterations of the Native Surface Oxide Film on 316L Austenitic Stainless Steel," J. Electrochem. Soc., **166**(11), pp. 3376–3388.

[97] Wang, L., Seyeux, A., and Marcus, P., 2020, "Ion Transport Mechanisms in the Oxide Film Formed on 316L Stainless Steel Surfaces Studied by ToF-SIMS with 18O2 Isotopic Tracer," J. Electrochem. Soc., **167**(10).

[98] Huang, X., Xiao, K., Fang, X., Xiong, Z., Wei, L., Zhu, P., and Li, X., 2020, "Oxidation Behavior of 316L Austenitic Stainless Steel in High Temperature Air with Long-Term Exposure," Mater. Res. Express, **7**(6).

[99] Wang, L., Seyeux, A., and Marcus, P., 2020, "Thermal Stability of the Passive Film Formed on 316L Stainless Steel Surface Studied by ToF-SIMS," Corros. Sci., **165**.

[100] Maurice, V., Peng, H., H. Klein, L., Seyeux, A., Zanna, S., and Marcus, P., 2015, "Effects of Molybdenum on the Composition and Nanoscale Morphology of Passivated Austenitic Stainless Steel Surfaces," Faraday Discuss., **180**(0), pp. 151–170.

[101] Raj, K. A., Arunkumar, M. P., Kanigalpula, P. K. C., and Karthikeyan, M., 2019, "Tribological and Vibrational Characteristics of AISI 316L Tested at Elevated Temperature and 600 Torr Vacuum," Def. Technol., **15**(1), pp. 58–64.

[102] O'Donnell, L. J., Michal, G. M., Ernst, F., Kahn, H., and Heuer, A. H., 2010, "Wear Maps for Low Temperature Carburised 316L Austenitic Stainless Steel Sliding against Alumina," Surf. Eng., **26**(4), pp. 284–292.
[103] Saka, N., Eleiche, A. M., and Suh, N. P., 1977, "Wear of Metals at High Sliding Speeds," Wear, **44**(1), pp. 109–125.
[104] Stack, M. M., Corlett, N., and Zhou, S., 1997, "A Methodology for the Construction of the Erosion-Corrosion Map in Aqueous Environments," Wear, **203–204**, pp. 474–488.
[105] Geringer, J., and Macdonald, D. D., 2012, "Modeling Fretting-Corrosion Wear of 316L SS against Poly(Methyl Methacrylate) with the Point Defect Model: Fundamental Theory, Assessment, and Outlook," Electrochimica Acta, **79**, pp. 17–30.
[106] Jian, S.-R., Teng, I.-J., Yang, P.-F., Lai, Y.-S., Lu, J.-M., Chang, J.-G., and Ju, S.-P., 2008, "Surface Morphological and Nanomechanical Properties of PLD-Derived ZnO Thin Films," Nanoscale Res. Lett., **3**(5), pp. 186–193.
[107] Chen, J., Shi, J., Wang, Y., Sun, J., Han, J., Sun, K., and Fang, L., 2018, "Nanoindentation and Deformation Behaviors of Silicon Covered with Amorphous SiO 2 : A Molecular Dynamic Study," RSC Adv., **8**(23), pp. 12597–12607.
[108] Zambrano, O. A., Coronado, J. J., and Rodríguez, S. A., 2015, "Mechanical Properties and Phases Determination of Low Carbon Steel Oxide Scales Formed at 1200°C in Air," Surf. Coat. Technol., **282**, pp. 155–162.
[109] Hu, Z., Ning, K., and Lu, K., 2016, "Study of Spark Plasma Sintered Nanostructured Ferritic Steel Alloy with Silicon Carbide Addition," Mater. Sci. Eng. A, **670**, pp. 75–80.
[110] Lacaze, J., and Sundman, B., 1991, "An Assessment of the Fe-C-Si System," Metall. Trans. A, **22**(10), pp. 2211–2223.
[111] Polmear, I., 2005, *Light Alloys: From Traditional Alloys to Nanocrystals*, Butterworth-Heinemann, Oxford.
[112] Porter, D. A., and Easterling, K. E., 1992, *Phase Transformations in Metals and Alloys, Third Edition (Revised Reprint)*, CRC Press, London.
[113] Smallman, R. E., and Bishop, R. J., 1995, *Metals and Materials: Science, Processes, Applications*, Butterworth-Heinemann, Oxford.
[114] Szewczyk-Nykiel, A., 2017, "Microstructure and Properties of Sintered Metal Matrix Composites Reinforced with SiC Particles," Tech. Trans., **114**(6), pp. 179–190.
[115] Sola, A., and Nouri, A., 2019, "Microstructural Porosity in Additive Manufacturing: The Formation and Detection of Pores in Metal Parts Fabricated by Powder Bed Fusion," J. Adv. Manuf. Process., **1**(3).
[116] Herzog, D., Seyda, V., Wycisk, E., and Emmelmann, C., 2016, "Additive Manufacturing of Metals," Acta Mater., **117**, pp. 371–392.
[117] Liverani, E., Toschi, S., Ceschini, L., and Fortunato, A., 2017, "Effect of Selective Laser Melting (SLM) Process Parameters on Microstructure and Mechanical Properties of 316L Austenitic Stainless Steel," J. Mater. Process. Technol., **249**, pp. 255–263.
[118] Reijonen, J., Revuelta, A., Riipinen, T., Ruusuvuori, K., and Puukko, P., 2020, "On the Effect of Shielding Gas Flow on Porosity and Melt Pool Geometry in Laser Powder Bed Fusion Additive Manufacturing," Addit. Manuf., **32**.
[119] Ahmed Obeidi, M., Mussatto, A., Groarke, R., Vijayaraghavan, R. K., Conway, A., Rossi Kaschel, F., McCarthy, E., Clarkin, O., O'Connor, R., and Brabazon, D.,

2020, “Comprehensive Assessment of Spatter Material Generated during Selective Laser Melting of Stainless Steel,” Mater. Today Commun., **25**.

[120] Obeidi, M. A., Conway, A., Mussatto, A., Dogu, M. N., Sreenilayam, S. P., Ayub, H., Ahad, I. U., and Brabazon, D., 2022, “Effects of Powder Compression and Laser Re-Melting on the Microstructure and Mechanical Properties of Additively Manufactured Parts in Laser-Powder Bed Fusion,” Results Mater., **13**.

[121] King, W. E., Barth, H. D., Castillo, V. M., Gallegos, G. F., Gibbs, J. W., Hahn, D. E., Kamath, C., and Rubenchik, A. M., 2014, “Observation of Keyhole-Mode Laser Melting in Laser Powder-Bed Fusion Additive Manufacturing,” J. Mater. Process. Technol., **214**(12), pp. 2915–2925.

[122] Gan, Z., Kafka, O. L., Parab, N., Zhao, C., Fang, L., Heinonen, O., Sun, T., and Liu, W. K., 2021, “Universal Scaling Laws of Keyhole Stability and Porosity in 3D Printing of Metals,” Nat. Commun., **12**(1).

[123] Wang, L., Mohammadpour, M., Yang, B., Gao, X., Lavoie, J.-P., Kleine, K., Kong, F., and Kovacevic, R., 2020, “Monitoring of Keyhole Entrance and Molten Pool with Quality Analysis during Adjustable Ring Mode Laser Welding,” Appl. Opt., **59**(6), pp. 1576–1584.

[124] Sokolov, M., Franciosa, P., Al Botros, R., and Ceglarek, D., 2020, “Keyhole Mapping to Enable Closed-Loop Weld Penetration Depth Control for Remote Laser Welding of Aluminum Components Using Optical Coherence Tomography,” J. Laser Appl., **32**(3).

[125] Wu, C., Jia, C., and Chen, M. A., 2010, “A Control System for Keyhole Plasma Arc Welding of Stainless Steel Plates with Medium Thickness,” Weld. J., **89**, pp. 225–231.

[126] Goncalves Assuncao, E., 2012, “Investigation of Conduction to Keyhole Mode Transition,” doctoral thesis, Cranfield University.

[127] Cherry, J. A., Davies, H. M., Mehmood, S., Lavery, N. P., Brown, S. G. R., and Sienz, J., 2015, “Investigation into the Effect of Process Parameters on Microstructural and Physical Properties of 316L Stainless Steel Parts by Selective Laser Melting,” Int. J. Adv. Manuf. Technol., **76**(5), pp. 869–879.

[128] Xiong, W., Hao, L., Li, Y., Tang, D., Cui, Q., Feng, Z., and Yan, C., 2019, “Effect of Selective Laser Melting Parameters on Morphology, Microstructure, Densification and Mechanical Properties of Supersaturated Silver Alloy,” Mater. Des., **170**.

[129] Song, B., Dong, S., and Coddet, C., 2014, “Rapid in Situ Fabrication of Fe/SiC Bulk Nanocomposites by Selective Laser Melting Directly from a Mixed Powder of Microsized Fe and SiC,” Scr. Mater., **75**, pp. 90–93.

[130] Gupta, M., Mohamed, F., and Lavernia, E., 1992, “The Effect of Ceramic Reinforcements during Spray Atomization and Codeposition of Metal Matrix Composites: Part II. Solid-State Cooling Effects,” Metall. Trans. A, **23**, pp. 845–850.

[131] Yin, Y. X., and Wang, H. M., 2005, “Microstructure and Wear Resistance of Cuss-Toughened Cr5Si3/CrSi Metal Silicide Alloys,” J. Mater. Res., **20**(5), pp. 1122–1130.

[132] Gao, C., Yao, M., Shuai, C., Peng, S., and Deng, Y., 2019, “Nano-SiC Reinforced Zn Biocomposites Prepared via Laser Melting: Microstructure, Mechanical Properties and Biodegradability,” J. Mater. Sci. Technol., **35**(11), pp. 2608–2617.

[133] Yang, Y., Cheng, Y., Peng, S., Xu, L., He, C., Qi, F., Zhao, M., and Shuai, C., 2021, “Microstructure Evolution and Texture Tailoring of Reduced Graphene Oxide Reinforced Zn Scaffold,” Bioact. Mater., **6**(5), pp. 1230–1241.

[134] Wang, H., and Zou, Y., 2019, "Microscale Interaction between Laser and Metal Powder in Powder-Bed Additive Manufacturing: Conduction Mode versus Keyhole Mode," Int. J. Heat Mass Transf., **142**.

[135] Papula, S., Song, M., Pateras, A., Chen, X.-B., Brandt, M., Easton, M., Yagodzinskyy, Y., Virkkunen, I., and Hänninen, H., 2019, "Selective Laser Melting of Duplex Stainless Steel 2205: Effect of Post-Processing Heat Treatment on Microstructure, Mechanical Properties, and Corrosion Resistance," Materials, **12**(15).

[136] Andreau, O., Koutiri, I., Peyre, P., Penot, J.-D., Saintier, N., Pessard, E., De Terris, T., Dupuy, C., and Baudin, T., 2019, "Texture Control of 316L Parts by Modulation of the Melt Pool Morphology in Selective Laser Melting," J. Mater. Process. Technol., **264**, pp. 21–31.

[137] Niendorf, T., Leuders, S., Riemer, A., Richard, H. A., Tröster, T., and Schwarze, D., 2013, "Highly Anisotropic Steel Processed by Selective Laser Melting," Metall. Mater. Trans. B, **44**(4), pp. 794–796.

[138] Liang, Y., Zhou, W., Liu, Y., Li, Z., Yang, Y., Xi, H., and Wu, Z., 2021, "Energy Absorption and Deformation Behavior of 3D Printed Triply Periodic Minimal Surface Stainless Steel Cellular Structures under Compression," Steel Res. Int., **92**(3).

[139] Dovgyy, B., Piglione, A., Hooper, P. A., and Pham, M.-S., 2020, "Comprehensive Assessment of the Printability of CoNiCrFeMn in Laser Powder Bed Fusion," Mater. Des., **194**.

[140] Salman, O. O., Brenne, F., Niendorf, T., Eckert, J., Prashanth, K. G., He, T., and Scudino, S., 2019, "Impact of the Scanning Strategy on the Mechanical Behavior of 316L Steel Synthesized by Selective Laser Melting," J. Manuf. Process., **45**, pp. 255–261.

[141] Qiu, C., Kindi, M. A., Aladawi, A. S., and Hatmi, I. A., 2018, "A Comprehensive Study on Microstructure and Tensile Behaviour of a Selectively Laser Melted Stainless Steel," Sci. Rep., **8**(1).

[142] Gu, D., Guo, M., Zhang, H., Sun, Y., Wang, R., and Zhang, L., 2020, "Effects of Laser Scanning Strategies on Selective Laser Melting of Pure Tungsten," **2**(2).

[143] Nong, X. D., and Zhou, X. L., 2021, "Effect of Scanning Strategy on the Microstructure, Texture, and Mechanical Properties of 15-5PH Stainless Steel Processed by Selective Laser Melting," Mater. Charact., **174**.

[144] Thijs, L., Kempen, K., Kruth, J.-P., and Van Humbeeck, J., 2013, "Fine-Structured Aluminium Products with Controllable Texture by Selective Laser Melting of Pre-Alloyed AlSi10Mg Powder," Acta Mater., **61**(5), pp. 1809–1819.

[145] AlMangour, B., Grzesiak, D., and Yang, J.-M., 2017, "Scanning Strategies for Texture and Anisotropy Tailoring during Selective Laser Melting of TiC/316L Stainless Steel Nanocomposites," J. Alloys Compd., **728**, pp. 424–435.

[146] Carter, L. N., Martin, C., Withers, P. J., and Attallah, M. M., 2014, "The Influence of the Laser Scan Strategy on Grain Structure and Cracking Behaviour in SLM Powder-Bed Fabricated Nickel Superalloy," J. Alloys Compd., **615**, pp. 338–347.

[147] Nadammal, N., Mishurova, T., Fritsch, T., Serrano-Munoz, I., Kromm, A., Haberland, C., Portella, P. D., and Bruno, G., 2021, "Critical Role of Scan Strategies on the Development of Microstructure, Texture, and Residual Stresses during Laser Powder Bed Fusion Additive Manufacturing," Addit. Manuf., **38**.

[148] Casati, R., Lemke, J., and Vedani, M., 2016, "Microstructure and Fracture Behavior of 316L Austenitic Stainless Steel Produced by Selective Laser Melting," J. Mater. Sci. Technol., **32**(8), pp. 738–744.

[149] Dryepondt, S., Nandwana, P., Fernandez-Zelaia, P., and List, F., 2021, "Microstructure and High Temperature Tensile Properties of 316L Fabricated by Laser Powder-Bed Fusion," Addit. Manuf., **37**.

[150] Pham, M. S., Dovgyy, B., and Hooper, P. A., 2017, "Twinning Induced Plasticity in Austenitic Stainless Steel 316L Made by Additive Manufacturing," Mater. Sci. Eng. A, **704**, pp. 102–111.

[151] Zhao, C., Bai, Y., Zhang, Y., Wang, X., Xue, J. M., and Wang, H., 2021, "Influence of Scanning Strategy and Building Direction on Microstructure and Corrosion Behaviour of Selective Laser Melted 316L Stainless Steel," Mater. Des., **209**.

[152] Chen, L., Richter, B., Zhang, X., Bertsch, K. B., Thoma, D. J., and Pfefferkorn, F. E., 2021, "Effect of Laser Polishing on the Microstructure and Mechanical Properties of Stainless Steel 316L Fabricated by Laser Powder Bed Fusion," Mater. Sci. Eng. A, **802**.

[153] Wang, D., Song, C., Yang, Y., and Bai, Y., 2016, "Investigation of Crystal Growth Mechanism during Selective Laser Melting and Mechanical Property Characterization of 316L Stainless Steel Parts," Mater. Des., **100**, pp. 291–299.

[154] Yin, Y. J., Sun, J. Q., Guo, J., Kan, X. F., and Yang, D. C., 2019, "Mechanism of High Yield Strength and Yield Ratio of 316 L Stainless Steel by Additive Manufacturing," Mater. Sci. Eng. A, **744**, pp. 773–777.

[155] Birnbaum, A. J., Steuben, J. C., Barrick, E. J., Iliopoulos, A. P., and Michopoulos, J. G., 2019, "Intrinsic Strain Aging, Σ3 Boundaries, and Origins of Cellular Substructure in Additively Manufactured 316L," Addit. Manuf., **29**.

[156] Sprouster, D. J., Streit Cunningham, W., Halada, G. P., Yan, H., Pattammattel, A., Huang, X., Olds, D., Tilton, M., Chu, Y. S., Dooryhee, E., Manogharan, G. P., and Trelewicz, J. R., 2021, "Dislocation Microstructure and Its Influence on Corrosion Behavior in Laser Additively Manufactured 316L Stainless Steel," Addit. Manuf., **47**.

[157] Zhong, Y., Liu, L., Wikman, S., Cui, D., and Shen, Z., 2016, "Intragranular Cellular Segregation Network Structure Strengthening 316L Stainless Steel Prepared by Selective Laser Melting," J. Nucl. Mater., **470**, pp. 170–178.

[158] Hettesheimer, T., Hirzel, S., and Roß, H. B., 2018, "Energy Savings through Additive Manufacturing: An Analysis of Selective Laser Sintering for Automotive and Aircraft Components," Energy Effic., **11**(5), pp. 1227–1245.